POWER: Preliminary Design of a Deployable 3U CubeSat for Microwave-Based Wireless Energy Recharge

Pierluca De Felice[1*†], Basilio Naclerio[1†], Francesca Vallozzi[1†], Elena Francesca Cipriano[2†], Pedro Jorge Duarte Correia[2†], Mélanie Ramarozatovo[3†], Romane Boussac[3†], Nicolás Tajuelo Arenas[4†], Marta Adalia Unzurrunzaga[4†], David López Rohde[4†]

[1*]Department of Aerospace Engineering, University of Naples "Federico II", Piazzale Tecchio, 80, Napoli, 80125, Italy.
[2]Department of Aerospace Engineering, Instituto Superior Técnico, Universidade de Lisboa, Av. Rovisco Pais, 1, Lisbon, 1049-001, Portugal.
[3]Department of Electronics and Electrical Engineering, École nationale supérieure d'électrotechnique, d'électronique, d'informatique, d'hydraulique et des télécommunications, 2 Rue Charles Camichel, Toulouse, 31000, France.
[4]Escuela Técnica Superior de Ingenieros Industriales, Universidad Politécnica de Madrid, C. de José Gutiérrez Abascal, 2, Chamartín, Madrid, 28006, Spain.

*Corresponding author(s). E-mail(s): pier.defelice@studenti.unina.it;
Contributing authors: b.naclerio@studenti.unina.it; f.vallozzi@studenti.unina.it; elena.f.cipriano@tecnico.ulisboa.pt; pedro.jorge.duarte.correia@tecnico.ulisboa.pt; melanie.ramarozatovo@inp-toulouse.fr; romane.boussac@etu.toulouse-inp.fr; nicolas.tajuelo@alumnos.upm.es; m.adalia@alumnos.upm.es; david.lopez.rohde@alumnos.upm.es;
†These authors contributed equally to this work.

Abstract

This paper presents the design of POWER (Platform for Orbital Wireless Energy Recharge), a 3U CubeSat mission developed to demonstrate microwave-based Wireless Power Transfer (WPT) in Low Earth Orbit. Aligned with UN Sustainable Development Goal 9, the mission addresses the critical limitation of satellite operational lifetimes imposed by onboard energy reserves, proposing a sustainable paradigm for in-orbit servicing. The project is the result of a multinational collaboration among four European universities (Naples Federico II, UPM Madrid, ENSEEIHT Toulouse, and IST Lisbon). The spacecraft architecture features a novel deployable payload system that separates a receiving module from the main bus while maintaining mechanical constraints, thus enabling controlled WPT experiments without the risks associated with autonomous formation flying. The payload integrates a custom-designed 5.2 GHz patch antenna array and a high-power density supercapacitor storage bank,

optimized to deliver high-current bursts required for transmission. This study details the mission analysis, subsystem design, and performance budgets, validating the feasibility of using compact CubeSat platforms to test technologies essential for future space-to-space energy distribution networks.

Keywords: CubeSat, Wireless Power Transfer (WPT), In-Orbit Servicing (IOS), Hybrid Energy Storage

1 Mission Description

This section outlines the primary operational framework of the POWER mission. It details the scientific objectives driving the system design, the alignment with international sustainability frameworks, and the comprehensive timeline from development to end-of-life disposal.

1.1 Mission Objective

POWER is a CubeSat in-orbit demonstration mission designed to investigate the feasibility of Wireless Power Transfer (WPT) between orbiting platforms. The primary objective is to validate the transfer of electrical energy in space, laying the foundation for future service satellites capable of recharging on-orbit assets. Such a capability would enable satellites to operate beyond their nominal lifetimes, reducing premature mission termination and contributing to a more sustainable use of the orbital environment by limiting the generation of space debris. POWER is conceived as a 3U CubeSat mission, specifically focused on the demonstration of space-to-space wireless energy transfer adopting a microwave-based approach, a technology that remains largely confined to experimental and research applications.

Fig. 1: POWER Mission Logo

At the current state of the art, the only in-space demonstrated heritage for microwave-based WPT is provided by the Caltech Space Solar Power Demonstrator-1 (SSPD-1), which included the MAPLE (Microwave Array for Power-transfer Low-orbit Experiment) payload. MAPLE successfully demonstrated that lightweight and flexible phased arrays are capable of transmitting power in the space environment, while also enabling an initial assessment of their performance and limitations. However, MAPLE was implemented on a 6U CubeSat architecture and operated as a hosted payload aboard the Vigoride-5 orbital transfer vehicle, relying on the host spacecraft for key subsystems such as attitude control, communications, and power supply [1]. In contrast, POWER represents a clear advancement over the current state of the art, as it is conceived as an independent nanosatellite mission dedicated exclusively to the demonstration of microwave-based space-to-space wireless power transfer, without reliance on a larger host platform.

Within the project, supercapacitors are adopted as a secondary energy storage system alongside conventional batteries. Supercapacitors are characterized by their ability to deliver energy significantly faster and with higher power density than traditional lithium-based batteries, while storing more energy than conventional capacitor [2]. Despite these advantages, several challenges remain, including lower overall energy density, voltage limitations, and a lower level of technological maturity compared to batteries. Nevertheless, as highlighted by the European Space Agency [3], supercapacitors are already being tested in space missions, demonstrating their strong potential for future high-power space applications. From an operational standpoint, the mission is constrained by the deployment of a single space segment, which precludes the launch and operation of two independent spacecraft. At the same time, the demonstration of wireless power transfer in orbit inherently requires precise relative positioning and stable face-to-face alignment between the

transmitting and receiving elements. To accommodate both the mission constraint and the physical requirements of microwave power transmission, POWER adopts a deployable module architecture in which a sub-module separates from the main 3U chassis after orbital insertion while remaining mechanically constrained through a guiding rail system. The module remains physically connected, as achieving and maintaining the required alignment through autonomous rendezvous and docking would introduce excessive complexity and risk, particularly at the nanosatellite scale. This configuration avoids the excessive complexity and risk of autonomous rendezvous and docking at the nanosatellite scale, enabling a controlled relative displacement while preserving the necessary alignment for the in-orbit demonstration.

1.1.1 Sustainable Developement Goals

The POWER mission is inherently aligned with the United Nations 2030 Agenda for Sustainable Development [4], utilizing technological innovation to promote a more efficient and responsible use of the orbital environment. The project primarily supports SDG 9 (Industry, Innovation, and Infrastructure) by validating a novel wireless power transfer (WPT) architecture that integrates microwave-based transmission with advanced supercapacitor storage, thereby promoting the development of resilient space infrastructure and enabling a transition from "disposable" satellite paradigms to a more sustainable model of in-orbit servicing. This effort naturally extends to SDG 7 (Affordable and Clean Energy), as the optimization of energy distribution through supercapacitors explores high-efficiency power management systems with potential spin-off applications for remote or wireless energy grids on Earth. Furthermore, by enabling in-orbit recharging and extending the operational lifespan of spacecraft, the mission directly contributes to SDG 12 (Responsible Consumption and Production), advocating for a circular space economy that reduces the frequency of replacement launches and mitigates the accumulation of space debris. This reduction in launch frequency also aligns with SDG 13 (Climate Action) by lowering the carbon footprint associated with space access, while simultaneously serving as a technical precursor for future Space-Based Solar Power (SBSP) systems critical for global carbon neutrality. Finally, the mission embodies SDG 17 (Partnerships for the Goals) through its multi-sectoral collaboration between academia, industry, and institutional stakeholders, facilitating the knowledge transfer necessary to advance international frameworks for sustainable space innovation.

1.2 Mission Phases and Mission Timeline

The POWER mission is scheduled for launch on 1st January 2030, with a nominal operational lifetime of one year. The mission lifecycle is structured into the following phases, following standard space project management frameworks:

- Phase A - PRE-DESIGN (September 2025-January 2026): The mission objectives were defined in alignment with UN Sustainable Development Goal 9 (Industry, Innovation, and Infrastructure). During this phase, the economic and technological feasibility was assessed, resulting in the preliminary conceptual design of the 3U CubeSat.
- Phase B - DEFINITION (January 2026 – June 2027): During this phase, the preliminary design of the satellite will be developed, and the optimal satellite configuration will be defined, including subsystem allocation and preliminary payload integration.
- Phase C - DETAILED DESIGN (June 2027-June 2028): The detailed design of the CubeSat will be carried out, including the selection of Commercial Off-The-Shelf (COTS) components for each subsystem, testing of the microwave antenna designed, refining structural and thermal designs, and preparing for system integration.
- Phase D - FULL SCALE DEVELOPEMENT (June 2028-December 2029): The spacecraft will be assembled and integrated, followed by functional, environmental, and performance testing to ensure mission readiness.
- Phase E - OPERATIONS (January 2030 – December 2030)
  - E1-Launch and Early Orbit Operations (1-2 weeks): Deployment into a Sun-Synchronous Orbit (SSO) at an altitude of 450 km. This phase includes detumbling, solar array deployment, and first contact with the ground

station. Systems checks will be performed to verify the health of all subsystems.
  - E2-Mission Operations and Experiment Execution (10-12 months): The core experimental phase follows a cyclical routine: the primary batteries recharge the supercapacitors for 40 minutes per orbit over four consecutive orbits, followed by a microwave power transmission event during the subsequent orbit. While multiple ground station contacts occur daily, data exchange is strategically limited to a single daily pass (approximately every 15 orbits) to optimize the power budget and streamline mission control operations. This window is used for the downlink of payload telemetry and experimental results.
  - E3-End of mission (January 2031-June 2032): Following the completion of the primary objectives, the satellite will enter a decommissioning state while its orbit naturally will decay.
- Phase F - DISPOSAL (June 2032): In strict compliance with international Space Debris Mitigation guidelines, the satellite will undergo atmospheric re-entry and incineration, ensuring no persistent debris remains in the LEO environment.

1.3 Concept Of Operations (ConOps)

The Concept of Operations (ConOps) describes the behavioral logic of the satellite, detailing how subsystems interact to perform mission tasks. This step is crucial for identifying critical phases and driving the design of the On-Board Data Handling (OBDH) and Electrical Power System (EPS). To this end, the operational modes defined in this iteration represent a preliminary approach to the POWER mission ConOps:

- **LEOP (Launch and Early Orbit Phase):** This mode is activated immediately upon spacecraft deployment. Its primary objectives are to detumble and stabilize the spacecraft, deploy the solar panels, and establish the first communication link with the ground station. During this phase, only platform-critical subsystems are active.
- **SAFE Mode:** This contingency mode is triggered autonomously by the On-Board Computer (OBC) in case of critical anomalies (e.g., low battery voltage, loss of attitude control). It prioritizes spacecraft survival by shedding non-essential loads.
- **RCG (Recharge):** This is the main operational mode. It assumes the platform bus is in idle state, while the payload recharges the Supercapacitors prior to the scientific demonstration. The RCG mode is planned to occur over multiple orbits in order to spread the power consumption and reduce the load on the power system.
- **SCI (Science Mode):** This mode entails testing the payload capabilities following the recharge phase. It is worth noting that the Science Mode relies solely on energy stored internally within the payload (supercapacitors) and does not draw power from the satellite's primary bus. Consequently, to simplify the representation, this mode has not been included in the power budget in Sec. 2.4.
- **RCG + DWN (Recharge + Downlink):** This mode mirrors the RCG state but accounts for the possibility of performing a downlink during the payload recharge phase within the same orbit.
- **DPL (Deploy):** A one-time operation during the mission. The payload deployment mechanism is activated to prepare for the second round of payload tests.

The mission execution follows a specific sequential logic based on these modes. Following the completion of LEOP, the spacecraft enters the nominal phase starting with the Payload Charging sequence (RCG/RCG+DWN), which spans multiple orbits to manage power loads. Once the payload is fully charged, the satellite transitions to Science Mode (SCI) to execute the wireless power transfer experiment, while simultaneously acquiring telemetry to verify system performance.

Upon completion of the experiment, the loop repeats. After a defined number of successful test cycles in the stowed configuration, the Deployment (DPL) mode is triggered to extend the payload structure. The mission then resumes the charging and testing cycles to characterize the power transfer efficiency at the increased distance.

Future developments may lead to a refinement of the system modes and operations.

1.4 Mission Analysis

A Low Earth Orbit (LEO) has been selected for POWER mission to achieve an optimal trade-off between the operational lifetime and European deorbiting regulations. The selection of orbital parameters is intended to maximize mission performance while ensuring full compliance with space debris mitigation guidelines.

1.4.1 The Orbit

POWER mission is defined as a scientific demonstration; it does not necessitate a specialized orbit or complex operational requirements, typically associated with Earth Observation missions. The design priorities are focused on achieving orbital simplicity and maximizing the energy collected by the satellite. Consequently, a Sun-Synchronous Orbit (SSO) with a 6 a.m. - 6 p.m. local time of ascending node is the best choice. This type of configuration allows the spacecraft to remain in nearly continuous sunlight, significantly reducing eclipse periods and providing a consistent power source while maintaining control over thermal variations. For a 6 a.m. – 6 p.m. SSO, the Sun is perpendicular to the orbital plane, optimizing satellite design: it is possible to make better use of solar panels, without requiring additional mechanisms to maximize sunlight exposure.

1.4.2 Orbit Parameters

The satellite will fly at an altitude (h) of 450 km. Taking into account the Mean Earth Radius ($R_\oplus$), the resulting semi-major axis (SMA) corresponds to the following:

$$a = h + R_\oplus \approx 6828 \text{ km} \tag{1}$$

The orbit is nearly circular, so the eccentricity can be approximated to zero:

$$e \approx 0 \tag{2}$$

Taking into account "$\mu_\oplus$" as the standard gravitational parameter for Earth, the orbital period can be determined using Kepler's Third Law:

$$\tau_0 = 2\pi\sqrt{\frac{a^3}{\mu_\oplus}} = 5615.14 \text{ s} = 93.59 \text{ min} \tag{3}$$

The SSO are nearly polar orbits. In this case, the inclination is equal to 97.2° and the analytical calculation [5] is provided below.

The first step is to impose the condition that the orbital plane precesses at the same rate as the Earth's revolution rate around the Sun. So, the angular velocity of the orbit's precession ω_p must equal the angular velocity of the Earth revolution motion around the Sun $\omega_r = \frac{2\pi}{\tau_\oplus}$.

For a circular orbit, ω_p is calculated as follows:

$$\omega_p = -\frac{3R_\oplus^2}{2a^2} J_2 \, \omega_{orbit} \cos(i) \tag{4}$$

where J_2 is the second zonal harmonic of Earth's gravitational potential that accounts for the Earth's equatorial bulge, approximately 1.082×10^{-3}.

Equating ω_r with ω_p, it is possible to obtain the inclination from the inverse formula:

$$i = \cos^{-1}\left(\frac{-2a^2\omega_p}{3R_\oplus^2 J_2 \, \omega_{orbit}}\right) = 97.2° \tag{5}$$

The same value is confirmed by the graph in Fig. 2 [6].

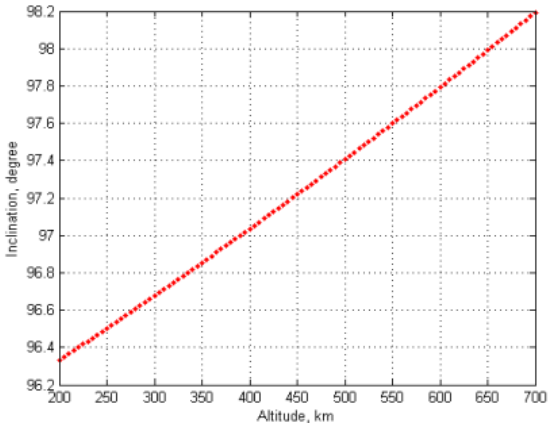

Fig. 2: Inclination required for an SSO at different altitudes.

The Right Ascension of the Ascending Node (RAAN) is functionally dependent on the initial epoch. Within this preliminary design phase, orbital injection is assumed to occur on January 1, 2030, at 00:00:00 UTC. Based on this reference launch date, the RAAN is determined to be 192.36°.

The True Anomaly (TA) and the Argument of Perigee (AOP) are instead considered equal to 0° at the beginning of the mission. In summary, the initial orbital parameters are presented in the table below.

Table 1: Orbital elements summary.

Parameter	Value
Altitude	450 km
SMA	6828.136 km
Eccentricity	0
Inclination	97.2 degrees
RAAN	192.36 degrees
AOP	0 degrees
TA	0 degrees
Epoch	01/01/2030 00:00:00
Orbital Period	5615.1 s

1.4.3 Mission Lifetime

The mission POWER has the main objective to be a platform for testing two distinct technologies: microwave power transmission and the application of supercapacitors in a space environment. Although the primary scientific demonstration for power transmission is estimated to require fewer than 15 orbits, approximately equivalent to one solar day, maintaining the CubeSat in orbit for an extended duration is considered essential.

A prolonged mission lifetime enables the execution of numerous demonstrations, facilitating a comprehensive evaluation of technological efficiency over time and the assessment of degradation levels resulting from exposure to the space environment. Furthermore, the European satellite decommissioning standards constitute a primary requirement. According to the Zero Debris approach of ESA [7], the deorbiting of the spacecraft must be completed within a five-year period from the initial mission epoch.

The NASA open-source General Mission Analysis Tool (GMAT) software has been used to evaluate the total mission duration. The orbital parameters were previously defined in Section 1.4.2, while the ballistic parameters are provided in Table 2.

Table 2: POWER's ballistic parameters.

Parameter	Value
DRY MASS	4.0 kg
DRAG COEFFICIENT	2.2
DRAG AREA	0.01 m^2
REFLECTIVITY COEFFICIENT	1.8
SRP AREA	0.09 m^2

The chosen dry mass has an average value between the mass without margins and the mass with margins indicated in Section 2.4; drag and reflectivity coefficients are typical values; drag and SRP area are evaluated considering the attitude of the satellite and the area of the solar panels. These values result in the following Ballistic Coefficient:

$$B = \frac{\text{Dry Mass}}{C_d \cdot A} = \frac{4.0}{2.2 \cdot 0.01} = 181.82 \text{ kg/m}^2 \quad (6)$$

With these parameters, it is estimated that the CubeSat will experience orbital decay after 1370 days from the launch date, which will occur on October 1, 2033. This timeframe aligns with international guidelines and ensures a successful mission.

Fig. 3 shows the variation of SMA over the elapsed days, during the entire lifetime.

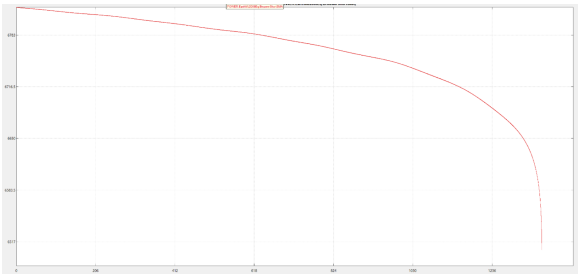

Fig. 3: SMA during POWER's decay.

2 Design Definition

This section provides a comprehensive overview of the POWER spacecraft design, moving from the high-level system architecture to the detailed physical configuration. The design strategy prioritizes the use of flight-proven Commercial Off-The-Shelf (COTS) subsystems for the bus, allowing the development effort to focus on the custom Wireless Power Transfer payload and its deployment mechanism. The following subsections detail the logical interfaces between components, the mechanical layout in both stowed and deployed configurations, and the consolidated system budgets (mass and power) that verify compliance with the mission constraints.

2.1 System description

Fig. 4 presents the block diagram of the system architecture, illustrating the interfaces between the various subsystems.

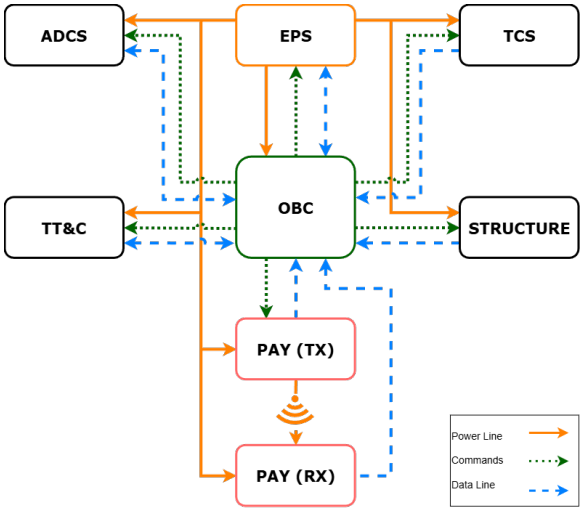

Fig. 4: POWER Block Diagram.

It is noteworthy that the Payload architecture is divided into two distinct modules. The Transmitting Unit (PAY TX) is powered directly by the EPS throughout the entire mission duration. In contrast, the Receiving Unit (PAY RX) is powered by the EPS only during the initial mission phases and immediately after payload deployment, primarily to execute system integrity checks. During science mode, the Receiving Unit is powered directly by the power transmitted from the Transmitting Unit. Command uplinks from the OBC are directed exclusively to the Receiving Unit for activation purposes. However, in terms of telemetry, both payload units interface directly with the OBC to transmit data lines during the Science Mode. Regarding the Thermal Control System (TCS), although the primary analysis focuses on passive solutions, provisions for power, command, and data lines have been included. This accounts for the internal thermal control elements embedded within individual subsystems, such as the temperature sensors on the OBC or the heaters integrated into the Battery Pack and allows for the potential future implementation of thermocouples on critical components for redundancy.

2.2 Equipment List and Structural Design

Table 3 presents the components selected for the POWER spacecraft. The majority of the selected items are Commercial Off-The-Shelf (COTS) units, a choice intended to ensure a reliable platform for the payload and mitigate the risk of system failures. The structural design is based on a standard 3U CubeSat structure manufactured by Endurosat.

To fulfill the specific mission objectives, a custom deployment mechanism has been designed. This system enables a configuration change, allowing for a second round of experiments with an increased distance between the wireless power transmitter and receiver. To facilitate this translation, the ASN22-130 Deploy Rail [8] (Fig. 5a) was selected, and a custom mechanical interface (Fig. 5b) was designed to integrate the rail with the primary satellite structure. The deploy rail connects directly to the Receiving Payload unit. Both the receiving and transmitting units are encapsulated within custom aluminum housings (Fig. 5c). Furthermore, the receiving housing is equipped with two A480-029-050 springs [9], which provide the necessary actuation force for deployment. Prior to activation, the Receiving Payload unit is retained in the stowed configuration by a burn wire mechanism. Fig. 5d shows the full integration of the payload structure in a deployed configuration.

To ensure reliable communication between the Receiving unit and the bus throughout the mission (in both stowed and deployed configurations),

Table 3: List of Components and Models per Subsystem.

Subsystem	Component	Model	No.
Structure	3U Structure	3U Cubesat Structure Endurosat	1
	Deploy Rail	ASN22-130	2
	Mechanism Structure	Custom	2
	Springs	A480-029-050	2
	Burn Wire	Custom	2
	Aluminium Panels	Custom	2
Payload	Supercapacitor	EATON TV1860-3R0107-R	8
	Variable Step-Down Reg.	LT3971	1
	Sync. Boost Converter	LTC3789	1
	VCO	FairView Microwave	1
	RF-to-DC (Rectenna)	Skyworks SMS7630	1
	DC/DC Converter	TPS6306x	1
	Transmitting Antenna	Custom	1
	Receiving Antenna	Custom	1
	Power Amplifier	ZVE-18GBX+	1
	Flat Cable	Cicoil	1
	Receiving Payload Box	Custom	1
	Transmitting Payload Box	Custom	1
ADCS	ADCS Box	TensorADCS-10m	1
EPS	Battery Pack	NanoPower BP4	1
	PCDU - Dock	NanoPower P60 Dock	1
	Array Conditioning Unit	NanoPower P60 ACU-200	1
	Power Distribution Unit	NanoPower P60 PDU-200	1
	Solar Panels	Endurosat Fixed Panel	1
	Solar Panels (deployed)	Endurosat Dbl Deployable	1
TT&C	Transceiver	Nanolink SDR S-Band	1
	Antenna	ISIS Space S-Band TT&C	1
OBDH	OBC	NanoMind A3200	1
TCS	TBD	—	—

a flat cable from Cicoil [10] is currently under evaluation. These cables are characterized by high durability, capable of withstanding tens of millions of flex cycles and radiation environments, while operating within a temperature range of -65 °C to 260 °C with low outgassing properties.

The remaining components listed in the table were selected to support the specific operational requirements of the POWER mission. A detailed discussion of the selection criteria for each subsystem is provided in Sec. 3.

2.3 Physical Configuration

Fig. 6 illustrates the satellite in its stowed configuration. Figs. 6a and 6b display all faces of the 3U CubeSat structure. The face housing the patch antenna is nadir-pointing, while the top 1U face corresponds to the Ram-facing side.

Figs. 6c and 6d provide a detailed view of the internal CubeSat configuration. Fig. 6c displays the stack from top to bottom, comprising: (1) the TensorTech 10m ADCS module; (2) the NanoPower P60 System (equipped with PCU, PDU, and the NanoMind A3200 OBC); (3) the NanoPower BP4 3000mAh battery pack; and (4) the NANOlink SDR S-Band Transceiver.

(a) ASN22-130 Rail

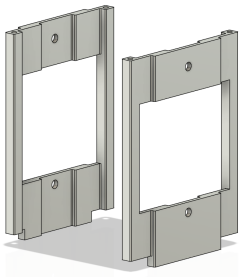

(b) Structure to rail mechanical interface

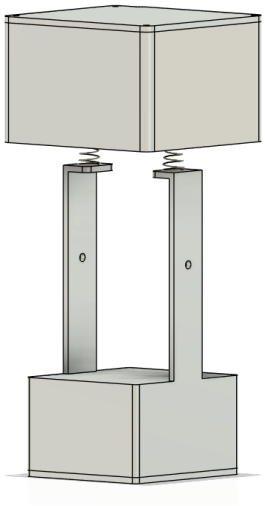

(c) Receiving (top) and Transmitting (bottom) boxes

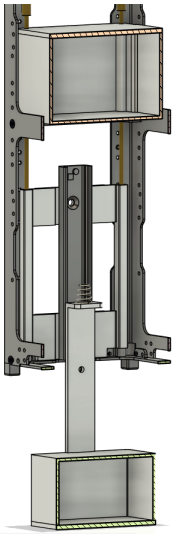

(d) Section of the deploy mechanism mounted the primary structure

Fig. 5: Deploy Mechanism

The payload layout can be schematized as follows: Transmitting Unit (5), Transmitting Antenna (6), Receiving Antenna (7), and Receiving Unit (8). Fig. 6d reveals the internal components of both the Payload Receiving and Transmitting units.

Finally, Figs. 7a and 7b present renderings of the fully deployed satellite, while Fig. 7c details the configuration of the deployed payload, highlighting the deployment mechanism and its interface with the main structure.

The requirement to integrate a deployable solar array resulted in a configuration that exceeds the mechanical envelope defined by the standard CubeSat Design Specifications (CDS). While the

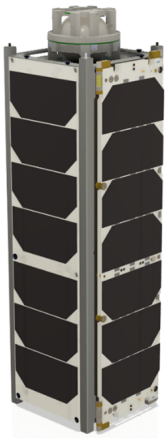

(a) Stowed configuration front

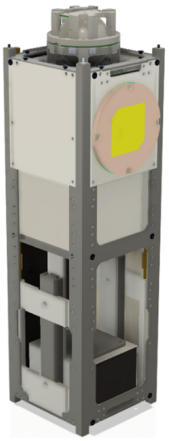

(b) Stowed configuration back

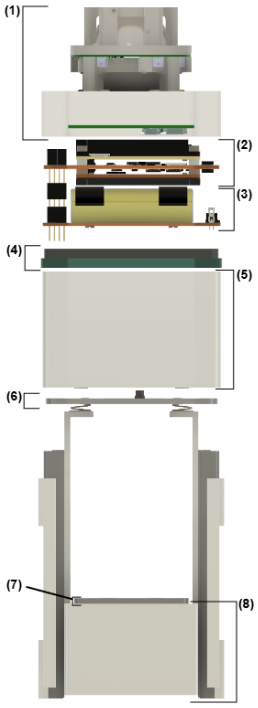

(c) Satellite details

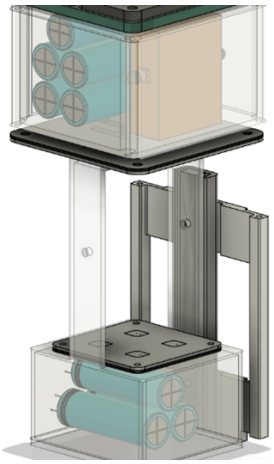

(d) Payload Detailed view

Fig. 6: POWER Satellite views: stowed configuration and internal details.

CDS limits protrusions on the X and Y faces to 6.5 mm [11], the EnduroSat Double Deployable Solar Panel creates a protrusion of 9.6 mm. This deviation renders the satellite incompatible with the

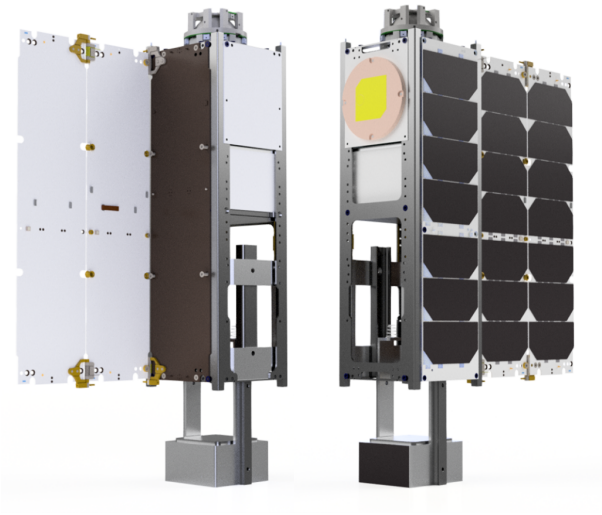

(a) Deployed configuration: front

(b) Deployed configuration: back

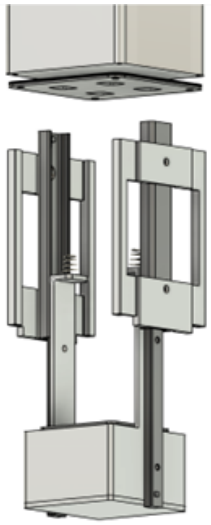

(c) Payload deployed view

Fig. 7: POWER Satellite views: Deployed configuration and Payload details.

majority of standard Commercial Off-The-Shelf (COTS) deployers.

Furthermore, the TensorTech 10m module protrudes from the Z-face of the CubeSat structure by approximately 32 mm, necessitating a deployer compatible with the so-called 'Tuna Can' volume extension.

Despite these geometric constraints, the POWER configuration remains compatible with

Fig. 8: Gauss Srl GPOD CubeSat Deployer

specific deployment systems, such as the GPOD manufactured by GAUSS Srl [12]. The GPOD is designed to accommodate lateral protrusions of up to 10 mm and provides an additional clearance of 36 mm along the Z-axis, effectively supporting the proposed 3U+ configuration.

2.4 System Budgets

In order to mitigate development risks, it is essential to identify and monitor the available margins at the system level. To this end, the IDM-CIC [13] tool was used to derive the Mass and Power budgets, allowing for a consolidated view of resource consumption. In accordance with the ESA IOD CubeSat Margin Policy [14], margins have been applied to each individual component based on its maturity. Additionally, an extra 8% has been added to the mass budget to account for the harness, following the ESA Margin philosophy for science assessment studies [15]. Finally, a 20% system margin has been included to account for the preliminary phase of the project.

Mass Budget

The computed mass budget is presented in Fig. 9. As illustrated, the total mass remains significantly below the maximum allowable limit for a 3U CubeSat, even when accounting for the system margin.

Power Budget

The Power Budget (Fig. 10) analysis computes the average power consumption by applying the Duty Cycle to each component over a typical orbit. The RCG + DWN mode has been identified as the sizing case due to its frequency and high power consumption; therefore, it was used for the preliminary estimation of the satellite power system in Chapter 3.4.

Mass Budget

Configuration : Reference

Payload

Target wet mass [Kg] : 2

Subsystem / Name	Quantity	Mass [Kg]	Margin [%]	Forced values Mass [Kg]	Forced values Margin [%]	Without margin [Kg]	Margin [%]	Margin [Kg]	Including margin [Kg]	% of total
Subsystem PAY						0.72	17.80%	0.13	0.84	22.12%
Supercap. EATON TV1860-3R0107-R	8	0.02	20.00%			0.16	20.00%	0.03	0.19	
Variable Step-Down Regulator LT3971	1	0.00	10.00%			0.00	10.00%	0.00	0.00	
Synchronous Boost Converter LTC3789	1	0.00	10.00%			0.00	10.00%	0.00	0.00	
RF-to-DC Conversion Stage Skyworks SMS7630	1	0.00	10.00%			0.00	10.00%	0.00	0.00	
Transmitting antenna	1	0.02	20.00%			0.02	20.00%	0.00	0.03	
Receiving antenna	1	0.02	20.00%			0.02	20.00%	0.00	0.03	
Power Amplifier ZVE-18GBX+	1	0.10	5.00%			0.10	5.00%	0.01	0.11	
Receiving Payload Box	1	0.18	20.00%			0.18	20.00%	0.04	0.21	
Transmitting Payload Box	1	0.23	20.00%			0.23	20.00%	0.05	0.27	
DC/DC Converter TPS6306x	1	0.00	10.00%			0.00	10.00%	0.00	0.00	
VCO	1	0.01	10.00%			0.01	10.00%	0.00	0.01	
Total dry mass without system margin						**0.72**	**17.80%**	**0.13**	**0.84**	
System margin							20.00%	**0.17**	**1.01**	
Total wet mass including all margins									**1.01**	

Bus

Target wet mass [Kg] : 4

Subsystem / Name	Quantity	Mass [Kg]	Margin [%]	Forced values Mass [Kg]	Forced values Margin [%]	Without margin [Kg]	Margin [%]	Margin [Kg]	Including margin [Kg]	% of total
Subsystem ADCS						0.50	5.00%	0.02	0.52	13.63%
TensorADCS-10m	1	0.50	5.00%			0.50	5.00%	0.02	0.52	
Subsystem PROP						0.00	0.00%	0.00	0.00	0.00%
Subsystem TTC						0.14	5.00%	0.01	0.15	3.86%
Nanolink SDR S-Band Transceiver	1	0.09	5.00%			0.09	5.00%	0.00	0.09	
ISIS Space S-Band Antenna	1	0.05	5.00%			0.05	5.00%	0.00	0.05	
Subsystem OBDH						0.02	5.00%	0.00	0.03	0.66%
NanoMind A3200	1	0.02	5.00%			0.02	5.00%	0.00	0.03	
Subsystem EPS						1.03	5.00%	0.05	1.08	28.44%
Battery (NanoPower BP4)	1	0.26	5.00%			0.26	5.00%	0.01	0.27	
PCDU Dock (NanoPower P60 Dock)	1	0.08	5.00%			0.08	5.00%	0.00	0.08	
ACU-200 NanoPower P60	1	0.05	5.00%			0.05	5.00%	0.00	0.06	
PDU-200 NanoPower P60	1	0.06	5.00%			0.06	5.00%	0.00	0.06	
Endurosat Double Deployable Array	1	0.44	5.00%			0.44	5.00%	0.02	0.46	
Endurosat Fixed Solar Panel	1	0.15	5.00%			0.15	5.00%	0.01	0.15	
Subsystem TCS						0.00	0.00%	0.00	0.00	0.00%
Subsystem STR						1.13	5.86%	0.07	1.19	31.28%
Endurosat 3U Structure	1	0.34	5.00%			0.34	5.00%	0.02	0.36	
Deploy Rail	2	0.17	5.00%			0.34	5.00%	0.02	0.36	
Springs	2	0.00	5.00%			0.00	5.00%	0.00	0.00	
Mechanism Support	2	0.06	20.00%			0.12	20.00%	0.02	0.15	
Aluminum Panel	2	0.01	20.00%			0.03	20.00%	0.01	0.03	
Burn Wire	2	0.01	20.00%			0.01	20.00%	0.00	0.01	
Harness (8% total mass)	1	0.28	0.00%			0.28	0.00%	0.00	0.28	
Total dry mass without system margin						**2.82**	**5.35%**	**0.15**	**2.97**	
System margin							20.00%	**0.59**	**3.56**	
Total wet mass including all margins									**3.56**	

System

	Without margin [Kg]	Margin [%]	Margin [Kg]	Including margin [Kg]
Total dry mass without system margins	**3.54**	**7.87%**	**0.28**	**3.81**
Total dry mass including system margins				**4.58**
Total propellant mass	**0.00**	**0.00%**	**0.00**	**0.00**
Total propellant mass including system margin		0.00%	**0.00**	**0.00**
Total wet mass including all margins				**4.58**

Fig. 9: IDM Mass Budget.

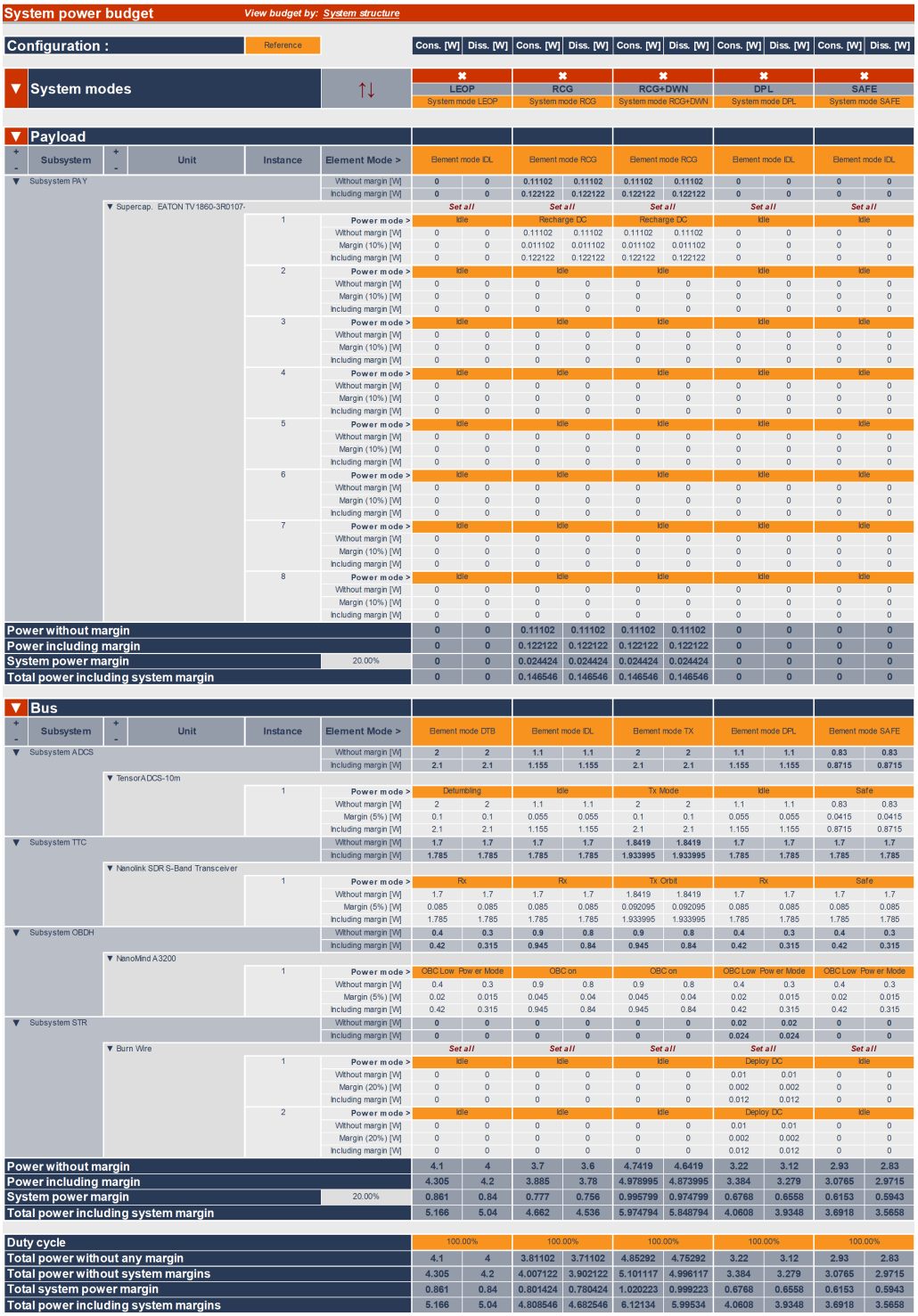

System power budget — *View budget by: System structure*

Configuration :	Reference	Cons. [W]	Diss. [W]	Cons. [W]	Diss. [W]	Cons. [W]	Diss. [W]	Cons. [W]	Diss. [W]	Cons. [W]	Diss. [W]
System modes		LEOP		RCG		RCG+DWN		DPL		SAFE	
		System mode LEOP		System mode RCG		System mode RCG+DWN		System mode DPL		System mode SAFE	
Payload											
Subsystem PAY	Without margin [W]	0	0	0.11102	0.11102	0.11102	0.11102	0	0	0	0
	Including margin [W]	0	0	0.122122	0.122122	0.122122	0.122122	0	0	0	0
Supercap. EATON TV1860-3R0107-		Set all		Set all		Set all		Set all		Set all	
1	Power mode >	Idle		Recharge DC		Recharge DC		Idle		Idle	
	Without margin [W]	0	0	0.11102	0.11102	0.11102	0.11102	0	0	0	0
	Margin (10%) [W]	0	0	0.011102	0.011102	0.011102	0.011102	0	0	0	0
	Including margin [W]	0	0	0.122122	0.122122	0.122122	0.122122	0	0	0	0
2	Power mode >	Idle		Idle		Idle		Idle		Idle	
	Without margin [W]	0	0	0	0	0	0	0	0	0	0
	Margin (10%) [W]	0	0	0	0	0	0	0	0	0	0
	Including margin [W]	0	0	0	0	0	0	0	0	0	0
3	Power mode >	Idle		Idle		Idle		Idle		Idle	
	Without margin [W]	0	0	0	0	0	0	0	0	0	0
	Margin (10%) [W]	0	0	0	0	0	0	0	0	0	0
	Including margin [W]	0	0	0	0	0	0	0	0	0	0
4	Power mode >	Idle		Idle		Idle		Idle		Idle	
	Without margin [W]	0	0	0	0	0	0	0	0	0	0
	Margin (10%) [W]	0	0	0	0	0	0	0	0	0	0
	Including margin [W]	0	0	0	0	0	0	0	0	0	0
5	Power mode >	Idle		Idle		Idle		Idle		Idle	
	Without margin [W]	0	0	0	0	0	0	0	0	0	0
	Margin (10%) [W]	0	0	0	0	0	0	0	0	0	0
	Including margin [W]	0	0	0	0	0	0	0	0	0	0
6	Power mode >	Idle		Idle		Idle		Idle		Idle	
	Without margin [W]	0	0	0	0	0	0	0	0	0	0
	Margin (10%) [W]	0	0	0	0	0	0	0	0	0	0
	Including margin [W]	0	0	0	0	0	0	0	0	0	0
7	Power mode >	Idle		Idle		Idle		Idle		Idle	
	Without margin [W]	0	0	0	0	0	0	0	0	0	0
	Margin (10%) [W]	0	0	0	0	0	0	0	0	0	0
	Including margin [W]	0	0	0	0	0	0	0	0	0	0
8	Power mode >	Idle		Idle		Idle		Idle		Idle	
	Without margin [W]	0	0	0	0	0	0	0	0	0	0
	Margin (10%) [W]	0	0	0	0	0	0	0	0	0	0
	Including margin [W]	0	0	0	0	0	0	0	0	0	0
Power without margin		0	0	0.11102	0.11102	0.11102	0.11102	0	0	0	0
Power including margin		0	0	0.122122	0.122122	0.122122	0.122122	0	0	0	0
System power margin	20.00%	0	0	0.024424	0.024424	0.024424	0.024424	0	0	0	0
Total power including system margin		0	0	0.146546	0.146546	0.146546	0.146546	0	0	0	0

Bus											
Subsystem ADCS	Without margin [W]	2	2	1.1	1.1	2	2	1.1	1.1	0.83	0.83
	Including margin [W]	2.1	2.1	1.155	1.155	2.1	2.1	1.155	1.155	0.8715	0.8715
TensorADCS-10m											
1	Power mode >	Detumbling		Idle		Tx Mode		Idle		Safe	
	Without margin [W]	2	2	1.1	1.1	2	2	1.1	1.1	0.83	0.83
	Margin (5%) [W]	0.1	0.1	0.055	0.055	0.1	0.1	0.055	0.055	0.0415	0.0415
	Including margin [W]	2.1	2.1	1.155	1.155	2.1	2.1	1.155	1.155	0.8715	0.8715
Subsystem TTC	Without margin [W]	1.7	1.7	1.7	1.7	1.8419	1.8419	1.7	1.7	1.7	1.7
	Including margin [W]	1.785	1.785	1.785	1.785	1.933995	1.933995	1.785	1.785	1.785	1.785
Nanolink SDR S-Band Transceiver											
1	Power mode >	Rx		Rx		Tx Orbit		Rx		Safe	
	Without margin [W]	1.7	1.7	1.7	1.7	1.8419	1.8419	1.7	1.7	1.7	1.7
	Margin (5%) [W]	0.085	0.085	0.085	0.085	0.092095	0.092095	0.085	0.085	0.085	0.085
	Including margin [W]	1.785	1.785	1.785	1.785	1.933995	1.933995	1.785	1.785	1.785	1.785
Subsystem OBDH	Without margin [W]	0.4	0.3	0.9	0.8	0.9	0.8	0.4	0.3	0.4	0.3
	Including margin [W]	0.42	0.315	0.945	0.84	0.945	0.84	0.42	0.315	0.42	0.315
NanoMind A3200											
1	Power mode >	OBC Low Power Mode		OBC on		OBC on		OBC Low Power Mode		OBC Low Power Mode	
	Without margin [W]	0.4	0.3	0.9	0.8	0.9	0.8	0.4	0.3	0.4	0.3
	Margin (5%) [W]	0.02	0.015	0.045	0.04	0.045	0.04	0.02	0.015	0.02	0.015
	Including margin [W]	0.42	0.315	0.945	0.84	0.945	0.84	0.42	0.315	0.42	0.315
Subsystem STR	Without margin [W]	0	0	0	0	0	0	0.02	0.02	0	0
	Including margin [W]	0	0	0	0	0	0	0.024	0.024	0	0
Burn Wire		Set all		Set all		Set all		Set all		Set all	
1	Power mode >	Idle		Idle		Idle		Deploy DC		Idle	
	Without margin [W]	0	0	0	0	0	0	0.01	0.01	0	0
	Margin (20%) [W]	0	0	0	0	0	0	0.002	0.002	0	0
	Including margin [W]	0	0	0	0	0	0	0.012	0.012	0	0
2	Power mode >	Idle		Idle		Idle		Deploy DC		Idle	
	Without margin [W]	0	0	0	0	0	0	0.01	0.01	0	0
	Margin (20%) [W]	0	0	0	0	0	0	0.002	0.002	0	0
	Including margin [W]	0	0	0	0	0	0	0.012	0.012	0	0
Power without margin		4.1	4	3.7	3.6	4.7419	4.6419	3.22	3.12	2.93	2.83
Power including margin		4.305	4.2	3.885	3.78	4.978995	4.873995	3.384	3.279	3.0765	2.9715
System power margin	20.00%	0.861	0.84	0.777	0.756	0.995799	0.974799	0.6768	0.6558	0.6153	0.5943
Total power including system margin		5.166	5.04	4.662	4.536	5.974794	5.848794	4.0608	3.9348	3.6918	3.5658

Duty cycle		100.00%		100.00%		100.00%		100.00%		100.00%	
Total power without any margin		4.1	4	3.81102	3.71102	4.85292	4.75292	3.22	3.12	2.93	2.83
Total power without system margins		4.305	4.2	4.007122	3.902122	5.101117	4.996117	3.384	3.279	3.0765	2.9715
Total system power margin		0.861	0.84	0.801424	0.780424	1.020223	0.999223	0.6768	0.6558	0.6153	0.5943
Total power including system margins		5.166	5.04	4.808546	4.682546	6.12134	5.99534	4.0608	3.9348	3.6918	3.5658

Fig. 10: IDM Power Budget.

3 Subsystems Design Definition

This section details the technical specifications and design choices for each functional subsystem of the POWER spacecraft. Following the system-level definition, the analysis proceeds with a dedicated focus on the custom Wireless Power Transfer payload, which drives the requirements for the supporting bus. Subsequent subsections describe the Telemetry, Tracking, and Command (TT&C) architecture, the On-Board Data Handling (OBDH) unit, the Electrical Power System (EPS), the Attitude Determination and Control System (ADCS), and the Thermal Control System (TCS). For each subsystem, the selection of components—primarily based on flight-proven COTS hardware—is justified against the specific mission requirements and environmental constraints identified in the previous phases.

3.1 Payload

The POWER mission payload constitutes a Microwave Wireless Power Transfer (WPT) In-Orbit Demonstrator (IOD). Its primary objective is to validate the complete energy transmission chain, encompassing the charging of the transmission source, the radiative transfer, and the subsequent recharging of the target storage device. To achieve this, the payload architecture is divided into two physically distinct modules: a Transmitting Unit and a Receiving Unit.

The operational sequence begins with the charging of the transmitter's internal energy buffer. Upon activation, the stored energy is converted into microwave radiation and directed toward the receiver. The Receiving Unit captures the RF signal, converts it back to Direct Current (DC), and recharges its local storage. This harvested energy is subsequently utilized to transmit experiment telemetry to the On-Board Computer (OBC) via a wired data link, continuing until the receiver's buffer is depleted. This cycle is repeated to gather statistical performance data. Following the initial test phase, the Receiving Unit is mechanically deployed to increase the separation distance, allowing for the characterization of transfer efficiency at a greater range. This design enables the in-situ verification of the WPT system, providing critical data to correlate on-orbit performance with theoretical models and ground-based tests.

3.1.1 Microwave Power Antenna Design

Functional overview of the RF power transfer chain

The RF payload is designed to demonstrate microwave power transfer between the two mechanically separated parts of the CubeSat platform. The objective is to transmit electromagnetic energy through free space and recover it as usable DC power at the receiving side. This process relies on a complete RF transmission and reception chain, coupled with a energy storage stage.

Microwave power transfer is achieved by radiating a radiofrequency signal through a transmitting antenna and collecting it using a receiving antenna. Antennas provide the essential transition between guided electromagnetic waves propagating in transmission lines and radiated waves propagating in free space. This conversion is reversible, allowing the received electromagnetic field to be transformed back into an RF signal at the receiver input.

Since microwave signals cannot be generated directly from a DC electrical source, an onboard RF generation stage is required. The RF signal is produced at the target frequency, conditioned to ensure spectral purity, amplified to the desired power level, and finally radiated by the transmitting antenna. On the receiving side, the collected RF power is delivered to an RF-to-DC conversion stage, where it is transformed into DC power and stored in supercapacitors. The present section focuses exclusively on the RF subsystem and does not address the DC storage architecture.

Fig. 11: Global chain of the microwave power transmission system

Frequency selection as the primary design parameter

The operating frequency critically determines antenna size and gain, which are essential for the microwave power transfer. Terrestrial demonstrations at 2.4 GHz (wavelength $\approx$ 12.5cm) required large antennas, such as 26m parabolic dishes, to achieve narrow beams and high gain—practical on Earth but incompatible with nanosatellite constraints.

At 5.2 GHz (wavelength $\approx 5.8cm$), compact patch antenna arrays can achieve high gain while fitting within typical CubeSat surfaces. This frequency enables efficient energy focusing and deployable integration without excessive system volume. Based on literature and space-oriented studies, the 5.2–5.8GHz band represents an optimal compromise between propagation efficiency, antenna miniaturization, and component availability. Consequently, 5.2GHz was selected as the reference frequency for the RF payload design [16].

RF generation and conditioning chain

The RF payload includes a complete signal generation and conditioning chain designed to deliver sufficient microwave power to the transmitting antenna while preserving signal stability and spectral purity.

- **RF Oscillator**: The RF oscillator converts DC electrical power into a stable sinusoidal signal at 5.2 GHz. It operates through a positive feedback mechanism in which an initial electrical perturbation is amplified until steady-state oscillations are established. The oscillation frequency is defined by a resonant element whose physical dimensions correspond to the wavelength at the operating frequency, approximately 5.8 cm.
  In this design, the oscillator delivers an output power of 20mW (10dBm), which is sufficient to drive the subsequent amplification stages. Harmonic components generated during the oscillation process will be suppressed using dedicated filtering to ensure compliance with spectral requirements and to prevent performance degradation in downstream components.
- **RF amplification and filtering** The RF chain includes filtering and amplification stages to raise the VCO output to the required transmission level. A band-pass filter with an insertion loss of 1.86dB is used to remove harmonics and ensure spectral purity. After filtering, the signal level entering the Power Amplifier (PA) is:

$$P_{LNA} = P_{VCO} - L_{VCO} - L_{filter} \approx 8.14\,\text{dBm} \quad (7)$$

This value is below the PA saturation limit of 12dBm, confirming that the PA input is within safe operating conditions. The PA provides a gain of 29dB and introduces an additional insertion loss of 0.4dB. The combination of these stages produces a transmitted RF power of approximately 9.44W, suitable for wireless power transfer over the short TX–RX distances considered.

Antenna selection and design

The antennas play a critical role in determining the efficiency of the microwave power transfer process. Antenna selection involves a trade-off between gain, directivity, losses, bandwidth, and mechanical integration constraints.

High-gain solutions such as horn antennas provide excellent radiation efficiency but are incompatible with the size constraints of nanosatellite platforms. Vivaldi antennas offer wide bandwidth and strong directivity, making them attractive candidates for wireless power transfer; however, their physical footprint and integration complexity remain challenging in a CubeSat context.

Thus, patch antenna arrays were selected for both the transmitting and receiving subsystems. Patch antennas offer a low-profile, lightweight, and planar structure that facilitates integration onto CubeSat surfaces. Additionally, patch elements can be efficiently combined into arrays to achieve high gain and controlled directivity without compromising mechanical simplicity.

In a rectangular microstrip patch antenna, electromagnetic waves propagate mainly in Transverse Magnetic (TM) modes within the cavity formed by the patch and the ground plane [17]. Each mode is characterized by a specific field distribution, with the dominant mode typically being the TM_{101} mode.

Radiation occurs primarily at the open edges of the patch, where the fringing fields are maximum and behave as radiating slots. Only modes that produce a non-zero tangential electric field at these edges effectively contribute to radiation [17]. Higher-order modes may also radiate, but they are

generally suppressed or avoided to ensure stable radiation patterns and efficient operation.

It is now possible to proceed with the design of the transmitting antenna. The patch (Fig. 12) dimensions are determined using formulas that ensure the desired propagation mode and resonance at the operating frequency.

$$W = \frac{v_0}{2f_r}\sqrt{\frac{2}{\epsilon_r + 1}} \tag{8}$$

$$L = \frac{1}{2f_r\sqrt{\epsilon_{eff}\epsilon_0\mu_0}} - 2\Delta L \tag{9}$$

With,

$$\epsilon_{eff} = \frac{\epsilon_r + 1}{2} + \frac{\epsilon - 1}{2}[1 + 12\frac{W}{h}]^{-\frac{1}{2}} \tag{10}$$

$$\frac{\Delta L}{h} = 0.412\frac{(\epsilon_{eff} + 0.3)(\frac{W}{h} + 0.264)}{(\epsilon_{eff} - 0.258)(\frac{W}{h} + 0.8)} \tag{11}$$

For an operating frequency of $f = 5.2\,\text{GHz}$, the optimized patch dimensions are $L = 19.1\,\text{mm}$ along the x-axis and $W = 14.7\,\text{mm}$ along y-axis.

The antenna is fed via a coaxial cable, which is inserted through the ground plane via a rear electronic board, not detailed in this document. Impedance matching to 50Ω is achieved by positioning the central conductor of the coaxial cable at the appropriate point on the patch, in accordance with the standard matching formula.

$$R(y) = R_{edge}cos(\frac{\pi y f_r}{L}) \tag{12}$$

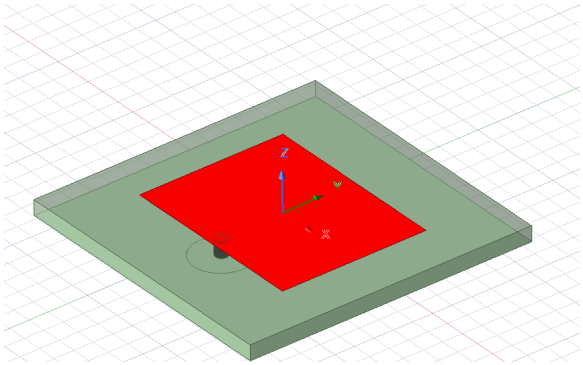

Fig. 12: Single antenna design

The performance of the single antenna are below.

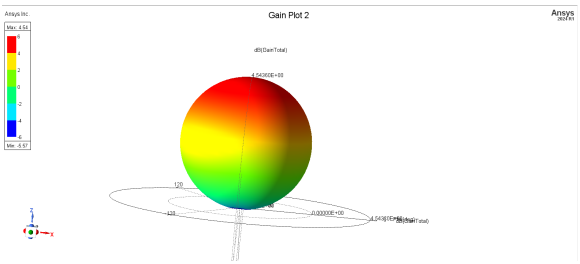

Fig. 13: Example of ideal patch antenna gain as a function of elevation and azimuth

A patch antenna gives a typical gain of 5dB-6dB.

The advantage of an antenna array lies in its ability to increase directivity along the axes of the elements arrangement. For example, when two antennas are aligned along the x-axis, the radiation pattern becomes narrower in that direction.

The expected gain for a network is given by the formula :

$$G_{array-dB} = G_{elements-dB} + 10log(N) \tag{13}$$

Electromagnetic simulations performed using HFSS software were used to design and optimize the transmitting antenna array represented on the figure below

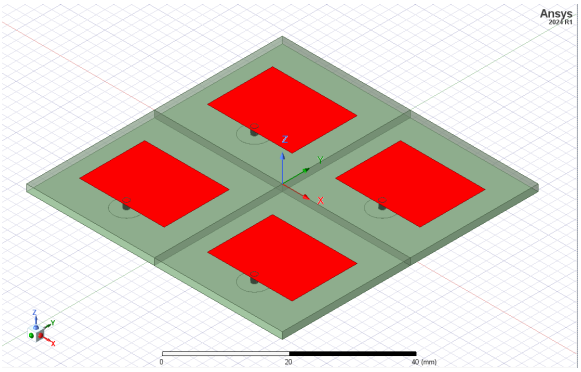

Fig. 14: View of the transmitting antenna array on HFSS

This is a feasibility study. The system provides sufficient gain to ensure transmission. Several strategies can be considered to improve performance. In addition, the spacing between the patches can be optimized. Other techniques, such as feed network phase shifting or the introduction of a vacuum gap between the radiating elements, represent potential improvements to the system [17].

With a better optimisation, the maximum gain increase, the main lobe is relatively wide, with limited gain degradation away from the boresight direction ($\theta = 0°$), which provides robustness against pointing inaccuracies and relative misalignments between the two satellite segments.

Rectenna selection and design

A rectenna is a device that captures ambient radio-frequency (RF) electromagnetic waves and converts them into usable electrical power. It combines an antenna that receives RF energy with a rectifier circuit that converts the alternating RF signal into a direct current (DC) output [18]. An impedance matching network is used between the antenna and the rectifier to maximize the power transfer. For this implementation, a patch antenna, an HF filter, a Schottky diode, and a DC filter were utilized.

The patch antenna design is presented below.

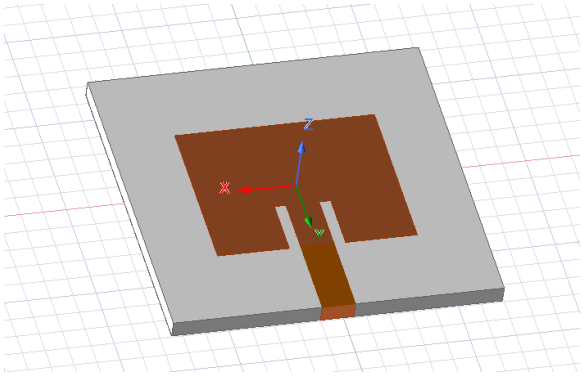

Fig. 15: Rectenna design

A gain of 6.59 was obtained, aligning with the desired specifications.

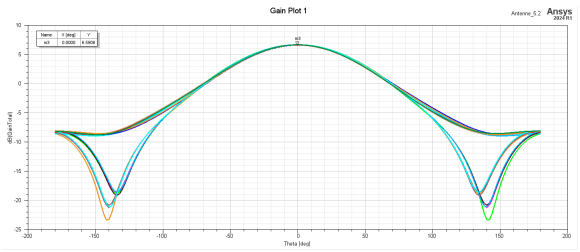

Fig. 16: Rectenna gain as a function of elevation

Subsequently, the signal undergoes processing through two distinct filtering stages. A 6th-order Butterworth low-pass filter with a cutoff frequency of 7.853GHz is employed to ensure minimal attenuation down to 5.2GHz. This component suppresses the harmonics generated by the diode and provides impedance matching between the conversion circuit (diode and DC filter) and the RF source (antenna) as illustrated below.

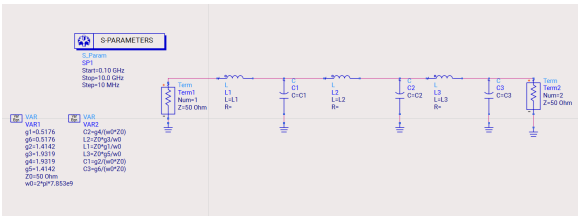

Fig. 17: Butterworth filter design on ADS

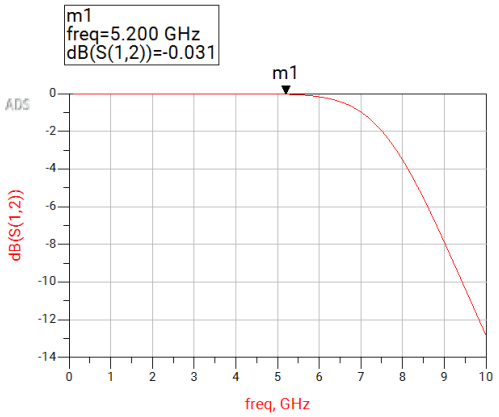

Fig. 18: Bode diagram of the Butterworth filter at 7.853 GHz

Another filter is implemented. A quarter-wave short-circuited stub is placed before the low-pass filter. At 5.2GHz, the stub behaves as an open circuit, preventing the DC component from reaching the RF source (antenna) and thereby avoiding unwanted radiation.

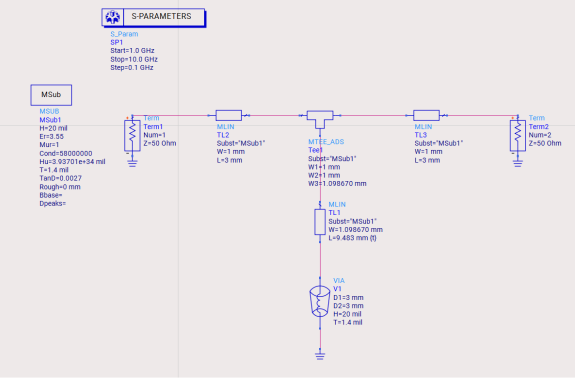

Fig. 19: High-pass filter design on ADS

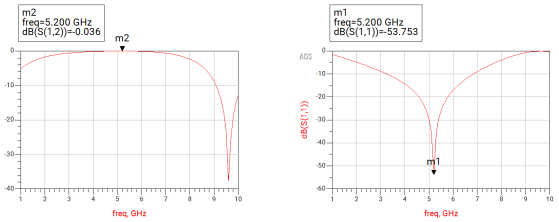

Fig. 20: High-pass filter simulation

Receiving-Side power budget and performance analysis

The received RF power is determined by the transmitted power, antenna gains, propagation distance, and system losses. The RF-to-DC conversion stage is characterized by a conversion efficiency of 50%, representing a realistic performance level for microwave rectification circuits.

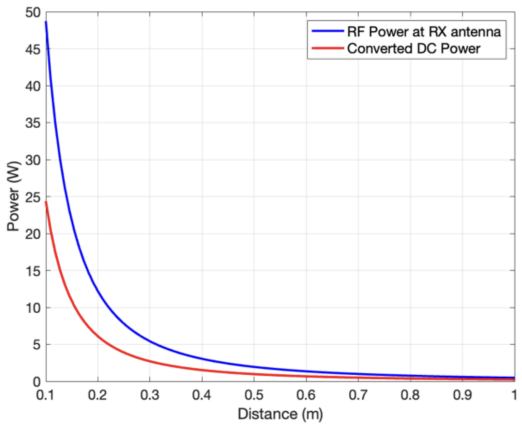

Fig. 21: RF received power and converted DC power vs distance

The RF payload performance was evaluated for two operational configurations corresponding to different distances between the transmitting and receiving subsystems: a stowed configuration (TX–RX separation: 110 mm) and a deployed configuration (TX–RX separation: 186 mm). The objective of this analysis is to quantify the impact of physical separation on received RF power and the corresponding DC power available for storage.

In both configurations, the RF chain was driven with the power amplifier input of 11.15 dBm, which is verified to be below the amplifier saturation limit. The transmitted RF power remained constant at 9.44 W.

- **Stowed Configuration (TX–RX Distance: 110 mm)** At a reduced separation distance, the receiving antenna captured a significant portion of the radiated RF power. The simulation results indicate:

Table 4: Power simulation at the output in stowed configuration.

Parameter	Value
RF received power (Pr)	40.3 W
DC power stored at the output	20.1 W

- **Deployed Configuration (TX–RX Distance: 186 mm)** In the deployed configuration, the increased separation distance leads

to a reduction in received power due to free-space propagation losses. Simulation results are presented in Tab. 5:

Table 5: Power simulation at the output in deployed configuration

Parameter	Value
RF received power (Pr)	14.1 W
DC power stored at the output	7 W

Despite the attenuation, the system still delivers a satisfying amount of energy.

These results confirm the feasibility of short-range microwave power transfer within a segmented CubeSat architecture and demonstrate that the recovered DC power is sufficient to support onboard energy storage.

3.1.2 Supercapacitor-Based Energy Buffer Design

The RF power transmission payload requires short, high-power bursts of 19.4 W. To meet this demand, a bank of supercapacitors was selected to power the POWER payload, employing an architecture that isolates the EPS battery. Supercapacitors were preferred over secondary batteries due to their suitability for power-dominant applications, providing high-power capability, long cycle life, thermal robustness, and reduced stress on the main battery. These advantages have driven interest in their implementation for high-power CubeSats; specifically, the adaptation of terrestrial COTS supercapacitors for space environments remains a key area of study [19].

Transmitting-Side Energy Buffer

The supercapacitor storage subsystem is dimensioned to sustain a 60-second transmission of 19.4 W at 16 V for the antennas, following the design methodologies outlined in [20]. To meet these requirements, a 5s1p configuration of Eaton TV1860-3R0107-R [21] cells was selected after simulating several models and configurations. The selection was based on mass, volume, and suitability criteria. Table 6 summarizes the primary technical features of this configuration.

Eaton TV supercapacitors are high-reliability EDLC energy storage devices using proprietary materials and processes. They offer ultra-high capacitance and ultra-low ESR for high power and energy density. With a 3.0 V operating voltage, they support backup, pulse, and hybrid power systems, alone or in combination with batteries. They are maintenance-free and designed for lifetimes up to 20 years; typical applications of the TV series include smart meters, RF pulse power, storage servers, industrial ride-through, and solar capture.

Fig. 22: Eaton TV1860-3R0107-R Supercapacitor cell.

Table 6: Technical Specifications for the EATON TV Supercapacitor Bank

Parameter	Value	Unit
Technology	EDLC	–
Configuration	5s1p	–
Capacitance (individual cell)	100	F
Total bank capacitance	12.60	F
String resistance	0.1103	Ω
Total bank power	503.2	W
Total bank energy	1298	J
Rated voltage (individual cell)	3	V
Total bank voltage	15	V
Mass (individual cell)	20	g
Total bank mass	100	g
Individual dimensions	⌀ 18.5 × 60.5	mm
Temperature range (T_{min}/T_{max})	−40/65	°C

Fig. 22 illustrates the TV1860-3R0107-R supercapacitor. Notably, the suitability of Eaton supercapacitors for space systems has already been demonstrated in previous studies [22].

Fig. 23 illustrates the simulated constant power discharge of the supercapacitor bank, transitioning from an initial voltage of 5 V to a cut-off

voltage of 5.4 V. A maximum current of 3.5 A is reached at the end of the discharge process.

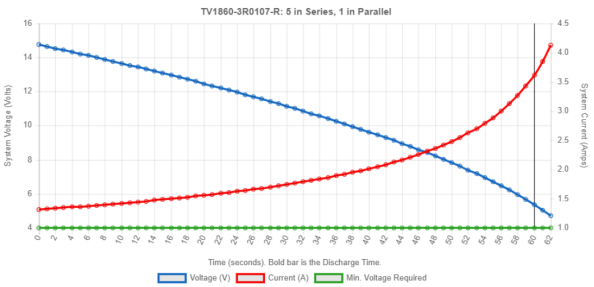

Fig. 23: Supercapacitor discharge simulation

The main auxiliary components to be designed include:

- **Charging regulator:** A constant-current/constant-voltage (CC-CV) buck converter utilizing the LT3971 [23] limits the charge current to 1.25 mA and 0.45 W. The total charging time follows the equation:

$$t_c = \frac{C}{I} \cdot \Delta V \tag{14}$$

  A full charge from zero requires approximately 166 minutes considering a total capacitance of 20 F (ideal capacitance for 5 supercapacitors of 100 F in series) and 101 minutes considering a capacitance at end of life of 12.6 F given by the supercapacitor manufacturer. The average power consumption in the charging process considering 90% efficiency is 0.26W. This charging approach ensures a controlled and safe charge of the five-cell series supercapacitor stack while minimizing stress, inrush current, and efficiency losses at low power levels. A simple buck topology is preferred over a buck-boost solution due to its lower quiescent consumption, reduced component count, and higher efficiency at low power.
- **Discharge regulator:** A high-efficiency (up to 98%) synchronous boost converter utilizing the LTC3789 [24] regulates the decaying capacitor voltage from 15 V to 5.4 V to a stable 16 V, 19.4 W output for the transmitting antenna during the 60 s experiment.
- **Safety & Support:** A passive cell-balancing circuit prevents individual supercapacitors from exceeding 3 V. External MOSFETs, a power inductor, and EMI filtering complete the design.

Receiving-Side Energy Harvesting & Storage

The receiving antenna, located on a deployable segment, harvests RF energy (simulated at 3.2 W). Its dedicated power system is a scaled-down version of the transmitter design:

- **RF-to-DC:** A Schottky diode (Skyworks SMS7630) rectenna converts received microwave power to DC.
- **Energy Buffer:** A 3S1P Eaton TV supercapacitor bank (100 F cells, 9 V total, 33.3 F effective) stores the harvested energy, providing over 1000 J of usable capacity.
- **Regulation:** A synchronous buck-boost converter (TPS63060) regulates the supercapacitor voltage (9.0 V to 4.5 V) to a stable 5 V output for telemetry electronics.

This optimized design minimizes mass (≈60 g) and volume for the deployable module while maintaining architectural consistency.

Advantages of CubeSat Integration

- **Thermal & Electrical Isolation:** The supercapacitor bank buffers the main EPS from high-power transients, enhancing overall system reliability.
- **Mass & Volume Efficiency:** The selected components provide the required peak power in a 1U-compatible form factor.
- **Space Environment Suitability:** The EDLCs operate across a wide temperature range (-40°C to +65°C), exhibit low outgassing, and are less susceptible to thermal runaway than batteries.

Contribution to Mission & Technology Demonstration

This energy storage subsystem enables the primary mission objective of demonstrating in-orbit wireless microwave power transmission. The use of supercapacitors is critical for managing the high peak-to-average power ratio of the RF payload. The design supports the broader mission goals of validating technologies for future distributed spacecraft, in-orbit servicing, and space-based power beaming architectures.

3.2 Telemetry, Tracking and Communications (TT&C)

The Telemetry, Tracking and Command (TT&C) subsystem is a fundamental element of the satellite communication architecture, as it ensures continuous monitoring of the satellite as well as enabling commanding from the ground station.

In this mission, the TT&C architecture is designed to be simple and robust, reflecting the low data-rate requirements. Unlike missions that generate large volumes of data (e.g., imaging payloads), the payload measurements considered here consist of low-rate numerical data. As a result, payload data can be transmitted together with telemetry and tracking information without the need for a dedicated high-throughput communication link.

Consequently, all data transmitted from the satellite to the ground station are grouped into a single downlink stream, which includes telemetry and tracking (housekeeping data, HK) and payload data. In contrast, command data are transmitted from the ground station to the satellite and therefore constitute a separate uplink, going from the ground station to the satellite.

The TT&C architecture operates in S-band, which is suitable for LEO missions and enabling compact spacecraft antennas while maintaining robust link margins with a high-performance ground station.

Space Segment Communication Hardware

The communication subsystem consists of an ISISPACE S-band patch antenna and a NANOlink SDR S-band transceiver (Figure 24). [25][26]

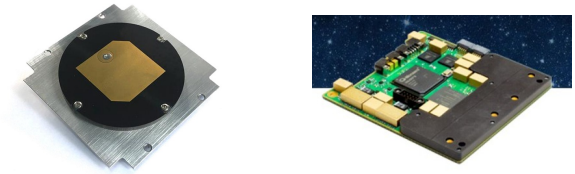

Fig. 24: Space segment communication hardware: (left) ISISPACE S-band patch antenna; (right) NANOlink SDR S-band transceiver. [25][26]

The patch antenna is a compact and lightweight, right-hand circularly polarized antenna operating in the 2200-2290 MHz frequency range, making it well suited for CubeSat S-band links. [26] The NANOlink SDR provides a flexible software-defined radio platform for S-band communications, enabling reliable telemetry and high-rate data transmission with configurable modulation and output power. [25]

Ground Segment

The Ground Segment is responsible for establishing and maintaining communication with the satellite in the mission lifetime. Its main functions include receiving downlinked data, monitoring spacecraft health and status (telemetry), supporting tracking operations, and transmitting commands to the satellite (uplink communication).

The main component of the Ground Segment is the Ground Station. For this mission, a single ground station approach has been adopted. This decision is justified by the relatively low data-rate requirements of the mission. Based on these considerations, Kiruna (Esrange), Sweden, was selected as the ground station supporting the mission. Kiruna is equipped with suitable radio-frequence (RF) infrastructure and able to work with S-band frequencies (the frequency used in this mission). [27]

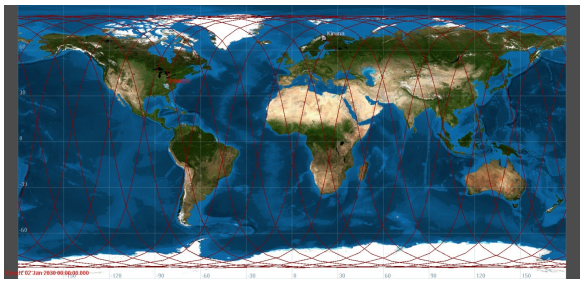

Fig. 25: World map showing the satellite ground track and its coverage relative to the Kiruna ground station.

The geographical coordinates for the Kiruna Ground Station are provided in the Table 7. These values are used consistently in communication and link budget simulations to ensure realistic geometry between the spacecraft and the ground station.

Table 7: Coordinates of the Kiruna Ground Station. [27]

Parameter	Value
Latitude	67° 53′ 22.410″ N
Longitude	21° 03′ 56.357″ E
Altitude	385.8 m

A contact analysis was performed using GMAT to evaluate the visibility between the satellite and the Kiruna ground station over a long-term operational period of approximately 400 days. The simulation results show that the satellite establishes frequent contact with Kiruna, with an average of about ten passes per day. The mean contact duration is approximately 366 s (around 6 minutes), which is sufficient for the transmission of the unified telemetry and payload data stream as well as for command operations. These results confirm that a single high-latitude ground station provides adequate coverage for the mission requirements.

Table 8: Values from the GMAT simulation.

Parameter	Value
Total number of contacts (N contacts)	3993
Average contacts per day	9.98
Average time in view per contact	366.4 s

Link Budget

A link budget quantifies whether the communication link between the satellite and the ground station is feasible by accounting for all gains and losses along the propagation path. The objective is to verify TT&C feasibility.

Following a standard CubeSat design workflow, the link budget was evaluated using the Satellite Link Budget Analyzer tool in MATLAB.

Two links were considered:

- L1 - Uplink Communication (Ground → Satellite) → Command data.
- L2 - Downlink Communication (Satellite → Ground) → Telemetry, tracking and payload data.

To start with, the housekeeping (HK) data per orbit is computed. Housekeeping telemetry is assumed to be transmitted in packets at a constant sampling frequency f. A typical packet size band sampling frequency are selected to represent periodic spacecraft status reporting. Using the orbital period obtained from GMAT, the volume of housekeeping data per orbit is given by the following equation. [28]

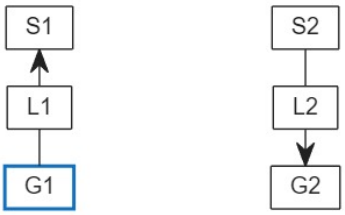

Fig. 26: Communication links.

$$D_{\mathrm{HK,orbit}} = b \cdot f \cdot T_{\mathrm{orbit}} \tag{15}$$

Assuming a packet size of 600 bits and a frequency of 0.1 Hz (one packet every 10 seconds), and considering the period of one orbit is $T_{\mathrm{orbit}} \approx$ 5670 s (from GMAT simulation):

$$D_{\mathrm{HK,orbit}} = 340.2 \text{ kb/orbit} \tag{16}$$

The payload data volume is negligible with respect to the HK data, so this is the total volume of the downlink communication link.

Finally, the minimum required data rate is estimated following the same approach adopted in the reference methodology:

$$R_{\mathrm{min}} = \frac{D \cdot M}{T_{\mathrm{use/orbit}}} \tag{17}$$

$$T_{\mathrm{use/orbit}} = \frac{N_c \left(F\, T_{\mathrm{avg}}\right)}{N_{\mathrm{orb/day}}} \tag{18}$$

,

where M accounts for operational margins, considered to be 3, F is the fractional reduction in viewing time in LEO (≈ 0.8), N_c is the average number of contacts per day, and T_{avg} is the average time in view per contact from GMAT. Using $N_c = 9.98$, $T_{\mathrm{avg}} = 366.4$ s, $N_{\mathrm{orb/day}} \approx 15.24$, $F = 0.8$, and $M = 3$, the resulting minimum data rate is $R_{\mathrm{min}} \approx 5.32$ kbps. Therefore, a design downlink data rate of 8 kbps is selected for the link budget analysis.

In order to correctly parameterize the link budget under realistic operating conditions, the geometric configuration between the spacecraft and the ground station at the beginning of a contact was analyzed using GMAT. The first acquisition

of signal (AOS) with the Kiruna ground station was identified at 01 Jan 2030 00:18:31.195 UTC.

The spacecraft Earth-fixed position at this first contact point was extracted from the GMAT simulation and converted to geodetic latitude and longitude. At the first contact with Kiruna, the CubeSat coordinates are approximately 70.90° N latitude and 65.81° E longitude.

The following analysis was carried out in the Satellite Link Budget Analyzer tool in MATLAB after computing the parameters needed and the results are the presented in Fig. 27.

Tag	Name	L1	L2
N1	Distance (km)	1.8572e+03	1.8572e+03
N2	Elevation (deg)	6.0526	6.0526
N3	Tx EIRP (dBW)	40.5000	-19.5000
N4	Polarization loss (dB)	3.0103	3.0103
N5	FSPL (dB)	164.6732	164.2691
N6	Received isotropic power (dBW)	-130.1835	-188.7794
N7	C/No (dB-Hz)	95.4157	61.8197
N8	C/N (dB)	55.4157	18.8094
N9	Received Eb/No (dB)	56.3848	22.7888
N10	Margin (dB)	45.3848	11.7888

Fig. 27: Numeric results from the link budget. [26]

Some assumptions regarding the spacecraft are still subject to refinement as the mission is still in pre-design phases. Therefore, the presented link budget results should be considered as representative estimates rather than final values. The objective of this analysis is to demonstrate the overall feasibility of the communication links between the spacecraft and the Kiruna ground station.

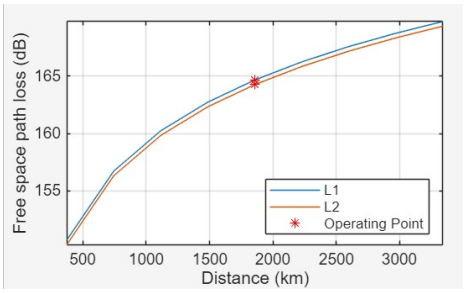

Fig. 28: Free-space path loss (FSPL) as a function of slant range for the uplink (L1) and downlink (L2).

The relationship between the free-space path loss (FSPL) and the slant range during a satellite pass is illustrated in Fig. 28, showing the expected increase in path loss as the distance between the satellite and the ground station grows, with a worst-case FSPL of approximately 165 dB at low elevation angles.

Additionally, the obtained results allow the evaluation of the link margin as a function of both transmission distance and transmitter output power, as depicted in Figs. 29 and 30. The uplink (L1) exhibits a significant positive margin, even under conservative assumptions such as low elevation angles and polarization mismatch losses, confirming the robustness of command transmission from the ground station. The downlink (L2), which is more critical due to the limited onboard transmission power, maintains a positive margin of approximately 12 dB, ensuring reliable data transmission throughout the pass.

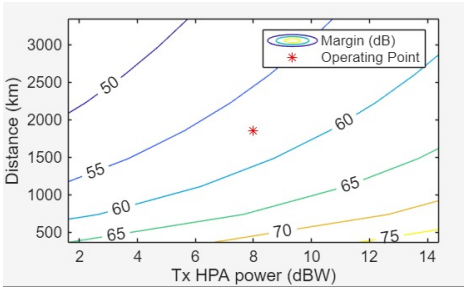

Fig. 29: Link margin (dB) as a function of transmitter HPA output power and distance for the uplink (L1).

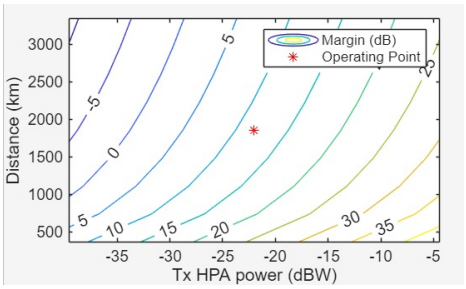

Fig. 30: Link margin (dB) as a function of transmitter HPA output power and distance for the downlink (L2).

These results confirm that, despite conservative assumptions on geometry and losses, the selected TT&C architecture can support reliable communication between the spacecraft and the ground segment.

3.3 On Board Data Handling (OBDH)

In contrast to missions that generate large volumes of data (e.g., imaging pay- loads), the POWER payload entails low-volume data exchange with the On-Board Computer (OBC), thereby relaxing the requirements for high-capacity storage and high-performance computing. Accordingly, the GomSpace NanoMind A3200 [29] has been identified as the optimal solution for the On-Board Data Handling (OBDH) subsystem.

The NanoMind A3200 is engineered for mission-critical applications and ensures operational resilience in harsh space environments (temperature range: -30°C to +85°C). Its compact form factor, combined with native compatibility with GomSpace NanoDock platforms, makes it particularly suitable for CubeSat architectures. Built upon the Atmel AT32UC3C 32-bit RISC MCU, the unit offers advanced power-saving features. Furthermore, the selection of a coherent hardware ecosystem reduces the risk of interface mismatch between the EPS and the OBDH subsystems during integration.

Fig. 31: GomSpace NanoMind A3200.

Regarding memory architecture, the OBC features 128 MB of NOR flash (split into two 64 MB dies for redundancy), 32 kB of FRAM for persistent configuration, and 32 MB of SDRAM. It also includes a Real-Time Clock (RTC) and onboard temperature sensors. To support Attitude Determination and Control System (ADCS) redundancy, the unit integrates a 3-axis magnetometer, gyroscopes, and three bidirectional PWM outputs. Connectivity is provided by dual I^2C buses, a CAN interface, SPI connectivity, and eight external Analog-to-Digital Converter (ADC) channels, configurable as General Purpose Input/Output (GPIO) for enhanced operational flexibility.

Regarding the Flight Software (FSW) architecture, NASA's F Prime (F´) [30] open-source framework is currently being evaluated as a primary candidate. This component-driven architecture is considered particularly suitable for the constrained resources of the NanoMind A3200, as it would allow for highly modular and reusable code development. The proposed adoption of F Prime is further motivated by its proven flight heritage (e.g., the Mars Ingenuity helicopter) and its native OS Abstraction Layer (OSAL), which facilitates integration with the underlying RTOS. Additionally, its embedded Ground Data System (GDS) would significantly streamline the Verification and Validation (V&V) phases.

3.4 Electrical Power (EPS)

Solar arrays constitute the primary energy source for both the payload and the spacecraft bus. The worst-case scenario for energy generation in a "SSO 6 a.m. - 6 p.m." occurs during the winter solstice, a period characterized by short and recurring eclipses. Electrical power is in any case supplied to the satellite using a battery. Comprehensive details regarding the Electrical Power Subsystem are provided within this section. The mathematical calculations and graph generation have been done through the support of a MATLAB script.

Solar arrays

The CubeSat is equipped with a combination of solar arrays provided by Endurosat: specifically, a "3U Double Deployable Solar Array" and a "3U Fixed Solar Array". The two components are illustrated in Fig. 32 and in Fig. 33. This configuration is mounted on the satellite face that is better exposed to the Sun, resulting in a final area of 9U. The complete configuration integrated into the CubeSat structure can be better examined in Section 2.1, where the CAD model is

presented. Technical specifications for these arrays are summarized in Table 9 [31].

Table 9: Endurosat solar arrays – Technical features.

Feature	Value
Number of cells	21
Efficiency at EOL	29+ %
Max Power in LEO	25.2 W
Mass	615 g
Max Voltage	17.5 V (for 7 cells)
Max Current	1.5 A

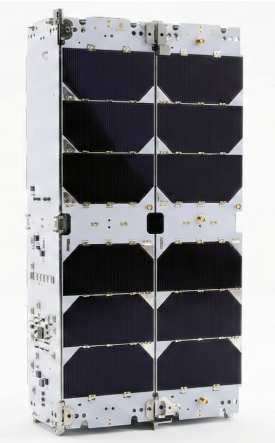

Fig. 32: 3U Double Deployable Solar Array.

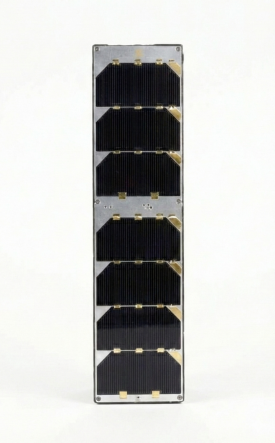

Fig. 33: 3U Fixed Solar Array.

According to the product datasheets, a nominal power of 25.2 W is specified. This value is considered a theoretical maximum and is subsequently adjusted in the following calculations to account for various efficiency factors and the effects of the solar incidence angle.

Battery

Another fundamental element of the Electrical Power Subsystem is the main battery. It represents a critical component of the spacecraft bus, as it provides power during eclipse periods and compensates for potential energy deficits during peak demand intervals.

The battery selected for the satellite is the "NanoPower BP4 3000mA", provided by GomSpace. It is a Lithium-Ion battery pack of 43Wh and represents a pragmatic choice for space applications, due to its advantageous high energy density characteristics, lightweight design, and flexibility [32].

Fig. 34: GomSpace - NanoPower BP4 3000mA.

Power Control and Distribution Unit (PCDU)

To enhance reliability and minimize integration risks, the PCDU components have been selected from the GomSpace ecosystem, ensuring full compatibility with the battery and the On-Board Computer. The system architecture is modular, based on the "NanoPower P60 Dock" backplane [33].

This mainboard hosts two specific daughterboards: the "P60 ACU-200" (Array Conditioning Unit) and the "P60 PDU-200" (Power Distribution Unit). The ACU integration ensures high efficiency through 6 independent Maximum Power Point Tracking (MPPT) channels, maximizing power extraction from the solar arrays [34]. The system provides regulated power buses and includes built-in over-current and over-voltage protections. Key specifications are listed in Table 10.

Table 10: PCDU P60 - System Specifications.

Parameter	Value
Product Series	NanoPower P60
Configuration	Dock + ACU-200 + PDU-200
Input Interface	6 MPPT Channels
Output Interface	9 Distribution Channels
Regulated Buses	3.3 V and 5.0 V
Op. Temperature	-35°C to +85°C
Interface	I^2C, CAN-Bus, UART

Power generation

The selected solar panels, including 21 cells, provide a nominal power output of 25.2 W. Starting from this baseline, the End-of-Life (EOL) operational power is determined, as the preliminary design is conducted in accordance with a worst-case scenario approach. Considering all the possible losses, the real value of the peak power is $P_{real} = 12.39$ W. In particular:

$$P_{real} = (\eta_{rad} \cdot \eta_{uv} \cdot \eta_{cy} \cdot \eta_{ad} \cdot \eta_{con} \cdot \eta_t \cdot H_I) \cdot P_{ideal} \quad (19)$$

where:

- $\eta_{rad} = (1 - 0.025)^{lifetime} = 0.90$. It accounts for the degradation during the total lifetime.
- $\eta_{uv} = 0.98$. It represents the effects of UV radiation.
- $\eta_{cy} = 0.99$. It accounts for thermal cycling.
- $\eta_{ad} = 0.75$. It includes assembly and design losses.
- $\eta_{con} = 0.99$. It refers to contamination from any sources.
- $\eta_t = 1 - 0.005(T - T_0) = 0.74$. It represents the effect of temperature variations experienced in the selected orbit.
- H_I is the solar constant correction factor (due to distance from Sun) and it is equal to 1, since the satellite is orbiting the Earth.

The effective power received by the solar panels must account for the incidence angle between the solar vector and the normal to the panel surface. Consequently, a final loss factor related to pointing is introduced: defining "α" as the angle of incidence, the pointing loss factor is expressed as $L_p = \cos(\alpha)$. The effective power obtained by the solar arrays is thus determined by the following relation:

$$P_{eff} = P_{real} \cdot L_p = P_{real} \cdot \cos(\alpha) \quad (20)$$

It is important to underline that the angle α is not constant but exhibits seasonal variations throughout the year. The next calculation has been conducted using a custom MATLAB script. Fig. 35 illustrates the variation of alpha starting from February 1, 2030, and covering exactly 1 year. Under optimal conditions, the panels are perfectly oriented toward the sun, such that $P_{eff} = P_{real}$. Conversely, the worst-case scenario occurs near the winter solstice and it is characterized by a maximum incidence angle of 34.7 degrees. The resulting trend for effective power is represented in Fig. 36.

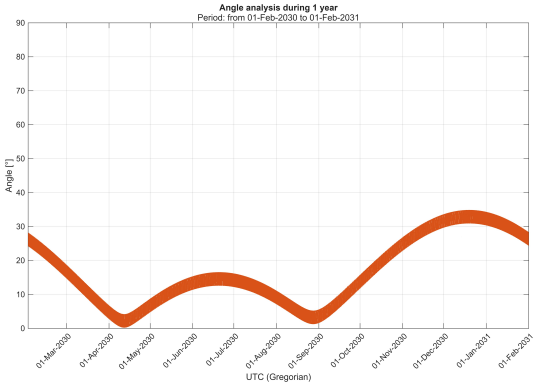

Fig. 35: Angle analysis during 1 year.

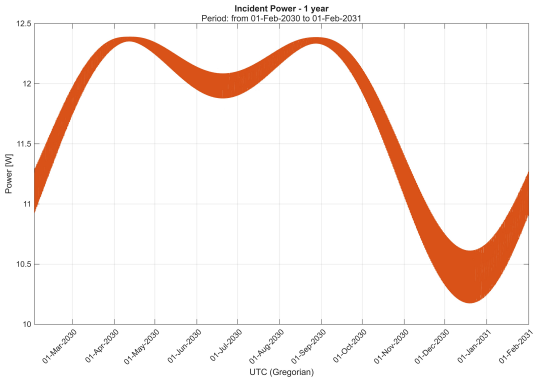

Fig. 36: Effective incident power during the year.

Power Consumption

Section 2.4 provides a detailed overview of energy consumption for each discrete component across the various mission phases. The On-Board Computer (OBC) and the Attitude Determination and Control Subsystem (ADCS) are categorized as permanently active, as these units are fundamental for maintaining spacecraft functionality and the required attitude orientation. Conversely, the remaining subsystems operate intermittently according to specific mission requirements. Table 11 summarizes the power consumption for the standard operational modes. These

Table 11: Power consumption for each component.

Subsystem	Mean Consumption	Idle	With Margin
OBC	0.9 W	Never	0.945 W
ADCS	2.0 W	Never	2.10 W
TTeC	5 W (Tx)	1.7 + 5% W (only Rx)	5.25 W
PAYLOAD	0.26 W	0 W	0.286 W

values incorporate the margins prescribed by the System Margin Policy [14]. Using this approach, the total power is further increased with a 20% margin.

Figure 37 illustrates the power consumption profile and the operational status of each subsystem over ten reference orbits, demarcated by green dashed vertical lines. Due to power generation constraints, a specific operational timeline was established for the payload and the Telemetry, Tracking, and Command (TT&C) subsystems.

The charging sequence for the supercapacitor requires a total duration of 160 minutes, which is divided into four 40-minute intervals at the commencement of the first four orbits. The fifth orbit is then dedicated to the discharge phase. Within the middle of the first orbit, the communication subsystem transmits signals to the ground station for a duration of 4 minutes, while the TT&C unit operates in an idle mode during the remaining periods.

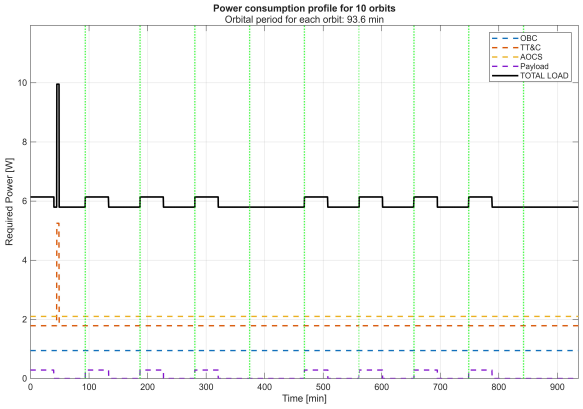

Fig. 37: Power consumption profile.

Battery: Charge and Discharge Cycle

It is essential to evaluate the battery discharge levels to ensure compliance with ESA guidelines, which require robust system margins to guarantee battery lifetime [35]. Consequently, a conservative Depth of Discharge (DoD) limit of 20% has been selected for the preliminary design. The State of Charge (SoC) has been determined through a MATLAB simulation, incorporating annual power generation data and the consumption profiles of the ten reference orbits.

The analysis focuses on the worst-case scenario during the winter solstice, characterized by eclipse periods of approximately 25 minutes. The results for two specific cases are illustrated in Fig. 38 and in Fig. 39: the first assumes a fully charged initial state (100% SoC), while the second considers an initial battery level of 85%.

In any case, the data demonstrates that the batteries return to a full state of charge within a single day, indicating no progressive discharge over time. The observed Depth of Discharge is notably low, at approximately 7%, which validates the suitability of the selected battery configuration. This performance level confirms that the power system can support nominal operations while maintaining a significant margin for emergency energy requirements or unforeseen losses not accounted for in the preliminary design.

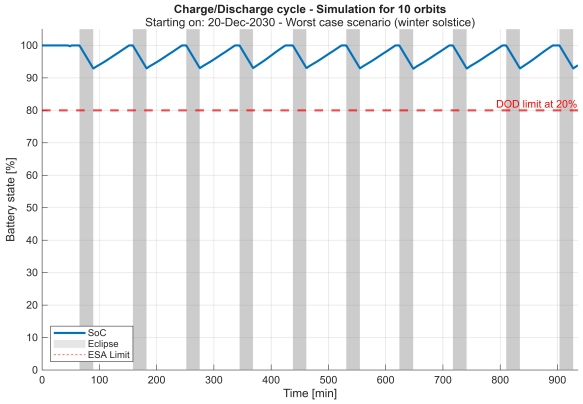

Fig. 38: State of Charge (SoC) - Initial state 100%.

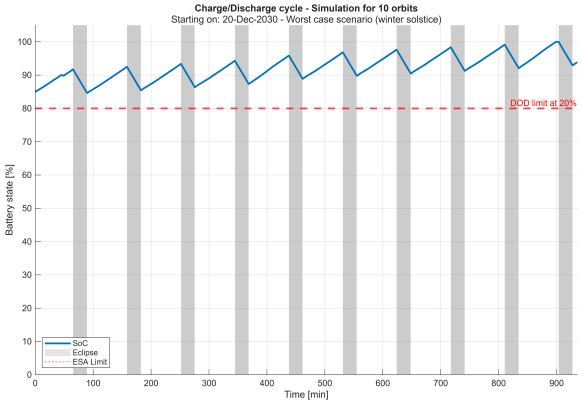

Fig. 39: State of Charge (SoC) - Initial state 85%.

3.5 Attitude Determination & Control (ADCS)

The POWER mission adopts three-axis stabilization with nominal nadir-pointing. The choice of attitude is mainly driven by the configuration of the double-deployable solar panels, which require a specific orientation to maximize electrical power generation efficiency throughout the orbit.

Unlike other WPT missions, pointing is not constrained by antenna alignment, since the coaxiality between transmitter and receiver is ensured by the mechanical constraint of the rail-based separation system. Therefore, the primary role of the ADCS is to maintain the satellite in an attitude that optimizes the energy balance (power-safe attitude) and ensures adequate thermal dissipation of the power components.

The performance requirements of the ADCS are:

- Pointing accuracy: A pointing accuracy of $\pm 2°$ is required. This margin is sufficient to keep the solar panels within an optimal efficiency range without overloading the actuators.
- Slew maneuvers: The operational phases of POWER require controlled reorientations for post-launch configuration and communications with ground stations. However, since the mission prioritizes the stability of nadir pointing for energy efficiency, high agility is not required. Consequently, the slew rate is limited to $0.1°/s$, a value that minimizes stress on flexible appendages and drastically reduces the instantaneous power consumption of the ADCS.

To size the control system, it is necessary evaluate the external and internal disturbance torques. To quantify the disturbances, the worst-case scenario was considered: namely the configuration with the solar panels deployed and the module separated along the rail.

3.5.1 Internal Disturbance

In the initial operational phase of the sub-module deployment, although the solar panels are already fully extended, a first-order approximation is adopted by assuming the satellite's Center of Mass (CoM) remains aligned with the translation axis of the deployable module. Under this assumption of transverse symmetry, the trajectory of the module from z_0 to z_{final} intersects the CoM, resulting in a null offset distance ($\mathbf{d}_{offset} = 0$). Consequently, no active torque is generated by the linear acceleration of the mass ($M_{trans} = 0$).

However, the time-dependent inertia tensor $\mathbf{I}(t)$ evolves during the translation, affecting the attitude dynamics. The governing equation for the spacecraft is expressed as:

$$\mathbf{M}_{ext} = \mathbf{I}(t)\dot{\boldsymbol{\omega}} + \boldsymbol{\omega} \times (\mathbf{I}(t)\boldsymbol{\omega}) + \dot{\mathbf{I}}(t)\boldsymbol{\omega} \qquad (21)$$

In a stabilized nadir-pointing attitude, where $\boldsymbol{\omega} \approx 0$, the primary effect of the translation is the modification of the gravity gradient stability margin and the required control gains. Nevertheless, an internal disturbance torque, M_{dyn}, arises if the spacecraft possesses even a minimal residual angular velocity $\boldsymbol{\omega}$. This torque is directly linked to the time-derivative of the inertia tensor $\dot{\mathbf{I}}(t)$. For the transverse axes (x, y), this variation is defined as:

$$\dot{I}_{xx} = \dot{I}_{yy} = 2 \cdot m_{mod} \cdot z(t) \cdot v_{rel} \qquad (22)$$

where $m_{mod} = 0.461$ kg is the mass of the moving module and v_{rel} is the separation velocity. The resulting dynamic disturbance torque is given by:

$$\mathbf{M}_{\text{dyn}} = \dot{\mathbf{I}}(t)\boldsymbol{\omega}(t) \qquad (23)$$

Assuming a nominal separation velocity $v_{rel} = 0.01$ m/s and a residual angular rate $\omega = 0.1°/s$ (typical of fine pointing phases), the peak disturbance is estimated at $1.57 \cdot 10^{-6}$ Nm. This value is an order of magnitude higher than the aerodynamic drag and comparable to the solar radiation pressure. The ADCS must actively compensate

for this transient internal effect to maintain the required pointing accuracy of $\pm 2^\circ$ during the entire separation maneuver.

3.5.2 Eternal Disturbances

The main external distourbances are:

Solar Radiation Pressure

The solar radiation pressure disturbance torque (M_s) is computed as:

$$\begin{aligned} M_s &= \frac{S}{c} A_s (1+q)(\mathrm{CSP}_s - \mathrm{CoM}) \cos(\theta) \\ &= 73.37 \cdot 10^{-8}\,\mathrm{N\ m} \end{aligned} \tag{24}$$

Table 12: Parameters for Solar Radiation Pressure torque

Parameter	Value
Solar constant (S)	$1361\,\mathrm{W/m^2}$
Speed of light (c)	$2.99 \cdot 10^8\,\mathrm{m/s}$
Sunlight surface (A_S)	$0.09\,\mathrm{m^2}$
Reflectance factor (q)	0.8
Distance between center of pressure and centre of mass ($CSP_s - CoM$)	0.1 m
Sun incidence angle (θ)	0°

Aerodynamic Drag

The aerodynamic drag disturbance torque (M_D) is computed as:

$$\begin{aligned} M_D &= \frac{1}{2}\rho V^2 C_D A_r (\hat{n}\cdot\hat{V}) \left[\hat{V} \times (\widehat{\mathrm{CSP}_s - \mathrm{CoM}})\right] \\ &= 2.44 \cdot 10^{-7}\,\mathrm{N\ m} \end{aligned} \tag{25}$$

Magnetic Field

The residual magnetic disturbance torque (M_m) is estimated as:

$$M_m = d \cdot B_0 = 7.68 \cdot 10^{-6}\,\mathrm{N\ m} \tag{26}$$

Table 13: Parameters for Aerodynamic Drag torque

Parameter	Value
Atmosphere density (ρ)	$3.8 \cdot 10^{-12}\,\mathrm{kg/m^3}$
Orbital velocity of the satellite (V)	7641 m/s
Drag surface (A_r)	$0.01\,\mathrm{m^2}$
Drag coefficient (C_D)	2.2
Distance between center of pressure and centre of mass ($CSP_s - CoM$)	0.1 m

Table 14: Parameters for Magnetic Field torque

Parameter	Value
Spacecraft residual dipole moment vector (m)	$0.3\,\mathrm{Am^2}$
Earth magnetic field (B_0)	$2.56 \cdot 10^{-5}\,\mathrm{T}$

Gravity Gradient

The gravity gradient torque ($\vec{M}_G$) acting on the CubeSat can be expressed as:

$$\vec{M}_G = \frac{3\mu}{r^3}\left[\hat{\mathbf{r}} \times (\mathbf{I}\cdot\hat{\mathbf{r}})\right] \tag{27}$$

By expressing the nadir direction $\hat{\mathbf{r}}$ in terms of the attitude angles α and β, the corresponding scalar components of the gravity gradient torque in the body reference frame are obtained as:

$$M_{G1} = \frac{3\mu}{r^3}(I_z - I_y)\,\sin\alpha\cos\alpha\cos^2\beta \tag{28}$$

$$M_{G2} = \frac{3\mu}{r^3}(I_z - I_x)\,\sin\beta\cos\beta\cos\alpha \tag{29}$$

$$M_{G3} = \frac{3\mu}{r^3}(I_z - I_y)\,\sin\alpha\sin\beta\cos\beta \tag{30}$$

The gravity gradient torque $\vec{M}_G$ is strongly dependent on both the spacecraft inertia distribution and its orientation with respect to the nadir vector. For the POWER mission, the *worst-case* configuration is defined as the condition in

which the sub-module reaches its maximum displacement (z_{final}), resulting in the highest inertia anisotropy.

The peak disturbance torque is analytically evaluated at the maximum allowable pointing error ($\alpha = 2°$), rather than at the theoretical equilibrium instability point of 45°, in order to reflect the operational constraints imposed by the ADCS. Under these conditions, the resulting gravity gradient torque magnitude is given by:

$$|\vec{M}_G| = \sqrt{M_{G1}^2 + M_{G2}^2 + M_{G3}^2} = 9.08 \times 10^{-9} \text{ N m} \tag{31}$$

Table 15: Parameters for Gravity Gradient torque

Parameter	Value
Moment of inertia x-axis (I_x)	0.0767 kg m^2
Moment of inertia y-axis (I_y)	0.1026 kg m^2
Moment of inertia z-axis (I_z)	0.0333 kg m^2
Gravitational constant of Earth (μ)	$3.986 \cdot 10^{14}$ m^3/s^2
Semi-major axis (r)	$6.828 \cdot 10^6$ m

Total external torque

The total external disturbance torque (M_{ext}) acting on the spacecraft is computed as the sum of the dominant environmental contributions:

$$M_{\text{ext}} = M_s + M_D + M_m + M_G = 8.01 \cdot 10^{-6} \text{ N m} \tag{32}$$

3.5.3 Detumbling

The detumbling control torque (M_d) required to dissipate the initial angular momentum within the allocated time interval ΔT is estimated as:

$$|M_d| = \frac{I_{\max}}{\Delta T} |\Delta\omega|_T \geq 4.78 \times 10^{-6} \text{ N m} \tag{33}$$

Assuming magnetic control, the corresponding required magnetic dipole moment ($d_{\text{detumbling}}$) can be derived from the relationship between control torque and geomagnetic field magnitude:

$$d_{\text{detumbling}} = \frac{M_d}{B_0} = 0.187 \text{ A m}^2 \tag{34}$$

Table 16: Parameters for Detumbling control torque

Parameter	Value
Maximum moment of inertia (I_{MAX})	0.1026 kg m^2
Orbital Period (ΔT)	5614.8 s
Difference between initial and final angular velocity ($\|\Delta\omega\|_T$)	0.2618 rad

3.5.4 Slew maneuver torque

The torque required to perform a slew maneuver depends on the target angular acceleration $\dot{\omega}$. According to the mission requirements, the slew rate is limited to $0.1°/s$. Assuming a ramp-up time of 10 s to reach this velocity, the required angular acceleration is $\dot{\omega} = 1.74 \cdot 10^{-4}\, rad/s^2$.

$$M_{\text{slew}} = I_{\text{MAX}} \dot{\omega}_{\text{slew}} = 1.79 \cdot 10^{-5} \text{ N m} \tag{35}$$

Table 17: Parameters for Slew Maneuver torque

Parameter	Value
Maximum moment of inertia (I_{MAX})	0.1026 $kg\ m^2$
Slew acceleration ($\dot{\omega}$)	$1.74 \cdot 10^{-4}\ rad/s^2$

3.5.5 Total angular momentum

The total angular momentum H_{tot} that the ADCS must manage is composed of the momentum required for nominal orbital rotation and the accumulation of environmental disturbances over a typical saturation period (usually one-quarter of an orbit).

$$H_{\text{tot}} = H_{\text{disturbances}} + H_{\text{rotation}} = 1.13 \cdot 10^{-2}\,\text{N m s} \tag{36}$$

Considering the nominal nadir-pointing rotation rate ($\omega_{orb} \approx 0.0011$ rad/s) and the integration of the maximum external torques, the requirements are calculated as follows:

$$H_{\text{rotation}} = I_{\text{MAX}}\omega_{\text{orb}} \approx 1.13 \cdot 10^{-4}\,\text{N m s} \tag{37}$$

Table 18: Angular Momentum Requirements

Parameter	Value
Nominal Angular Momentum (H_{nom})	$1.13 \cdot 10^{-4}$ Nms
External Disturbances integration (per quarter-orbit)	$1.12 \cdot 10^{-2}$ Nms

3.5.6 ADCS Hardware Selection: TensorADCS-10m

The TensorADCS-10m (see Fig. 40) is an integrated Attitude Determination and Control System (ADCS) designed for nano-satellites, featuring an architecture optimized to minimize power consumption while providing high agility through Control Moment Gyroscope (CMG) technology.

The system employs a comprehensive suite of sensors for precise satellite state determination:

- 6× **TensorFSS-15M**: six Fine Sun Sensors that provide 4π coverage for vector determination with high precision.
- **ADCS-MCB (Inertial Suite):** The main control board integrates a 3-axis MEMS gyroscope and a digital magnetometer to monitor angular rates and the local magnetic field vector.

Attitude control is achieved through a combination of mechanical and electromagnetic actuators:

- 2× **TensorMTQ-200m (integrated with ADCS-MCB)**: Integrated electromagnetic coils that interact with the Earth's magnetosphere. The MTQ-200m units handle the X and Y axes.

Fig. 40: TensorADCS-10m

- **Air-Coil (integrated with ADCS-MCB)**: Integrated electromagnetic coils that interact with the Earth's magnetosphere.The Air-Coil manages the Z-axis.
- 2× **TensorCMG-10m-N**: Two Control Moment Gyroscopes serve as the primary actuators. They exploit the gyroscopic effect by tilting a spinning rotor's momentum vector, providing high torque efficiency for fine pointing.

The TensorADCS-10m is therefore a suitable and high-performance hardware choice to support the operational requirements of the POWER mission.

3.6 Thermal Control (TCS)

The thermal control analysis was conducted in three sequential steps, with each step building on and refining the results of the previous one. The analysis initially employed an in-house MATLAB code, while the final results were obtained using the MATLAB CubeSat Thermal Power Toolbox. The heat sources considered throughout the analysis include direct solar radiation, Earth infrared radiation, and albedo effects; internal heat generation was additionally accounted for in the Thermal Toolbox simulations. For the on-orbit thermal exchange mechanisms, the satellite is assumed to operate in a vacuum environment; therefore, convective heat transfer is neglected. Heat exchange between the spacecraft and the external environment is assumed to occur exclusively through radiation, while internal heat transfer is dominated by conduction, with radiative exchange also considered.

In the preliminary phase of the analysis, the steady-state temperature of the satellite external surfaces is estimated. This temperature is

Table 19: Comparison between POWER mission requirements and TensorADCS-10m performance specifications.

Parameter	Requirement	TensorADCS-10m Specification	Outcome
Pointing Accuracy	$\pm 2^\circ$	0.4° (Typical)	Satisfied
Maximum Torque	$1.79 \cdot 10^{-5}$ Nm	$1.0 \cdot 10^{-3}$ Nm	Satisfied
Angular Momentum (H)	$1.13 \cdot 10^{-2}$ Nms	$1.3 \cdot 10^{-2}$ Nms	Satisfied
Slew Rate	$0.1^\circ/s$	$5^\circ/s$	Satisfied
Detumbling (Dipole)	0.187 Am^2	0.2 Am^2 (X/Y) + 0.1 Am^2 (Z)	Satisfied

obtained by imposing a global thermal balance, equating absorbed and emitted thermal power densities under a set of simplifying assumptions. An essential satellite model is adopted, in which the overall geometry of a 3U cubesat is preserved while each surface is assumed to be either fully illuminated or fully in eclipse. The satellite is further assumed to be isothermal, with no internal thermal exchanges modeled. This preliminary analysis defines the conservative thermal bounds for the spacecraft, the two worst-case thermal scenarios: the worst-case cold condition, corresponding to the minimum expected temperature in the absence of external heat sources, and the worst-case hot condition, corresponding to the maximum expected temperature.

As a second step, the in-house MATLAB code refines the analysis by predicting the satellite temperature time history over the first year of the POWER mission, using the orbital evolution to compute the effective incidence of the external heat fluxes on the spacecraft surfaces. Consequently, the model captures not only the sunlit-eclipse alternation but also the gradual seasonal variation of the temperature maxima and minima.

The temperature is obtained by solving the transient energy balance,

$$mc\,\frac{dT}{dt} = \dot{Q}_{\text{in}}(t) - \dot{Q}_{\text{out}}(t), \tag{38}$$

which is numerically integrated in time (Euler scheme) as

$$T_{k+1} = T_k + \frac{\left(\dot{Q}_{\text{in},k} - \dot{Q}_{\text{out},k}\right)\Delta t_k}{mc}. \tag{39}$$

In the model, the net incoming heat rate is expressed as

$$\dot{Q}_{\text{in}}(t) = \dot{Q}_{\odot}(t) + \dot{Q}_{\text{alb}} + \dot{Q}_{\text{IR}}, \tag{40}$$

where the absorbed direct solar contribution is computed as

$$\dot{Q}_{\odot}(t) = \alpha_{\text{p}}\, S\, A_{\text{p}}\, \cos\theta(t)\, f_{\text{sun}}(t), \tag{41}$$

with $f_{\text{sun}}(t) \in \{0, 1\}$ accounting for eclipse periods, and $\theta(t)$ obtained from the instantaneous Sun–spacecraft geometry. The albedo and Earth infrared contributions are modelled as constant terms in this intermediate step, consistent with the adopted assumptions. Heat rejection to deep space is represented by radiative emission,

$$\dot{Q}_{\text{out}}(t) = \dot{Q}_{\text{rad}}(t) = \epsilon_{\text{eq}}\, A_{\text{eq}}\, \sigma \left(T^4 - T_{\text{space}}^4\right). \tag{42}$$

In this intermediate model, thermally relevant parameters (e.g. absorptivity and emissivity) and the solar constant are assumed time-invariant, and the results depend on the assumed initial temperature ($T_0 = 300K$). Internal heat generation and heat exchange between internal components or facing surfaces are not included at this stage.

The initial thermal computations were performed for two representative surface finish configurations. In the first case, the spacecraft was assumed to be entirely covered with polished aluminum, characterized by an absorptivity $\alpha = 0.15$ and an emissivity $\epsilon = 0.05$. As expected, this configuration resulted in relatively high temperatures, due to the limited radiative heat rejection capability associated with low-emissivity surfaces (Fig. 41).

To investigate a more realistic configuration, a second simulation was conducted assuming all external surfaces to be coated with a black thermal coating, with $\alpha = 0.96$ and $\epsilon = 0.91$. This

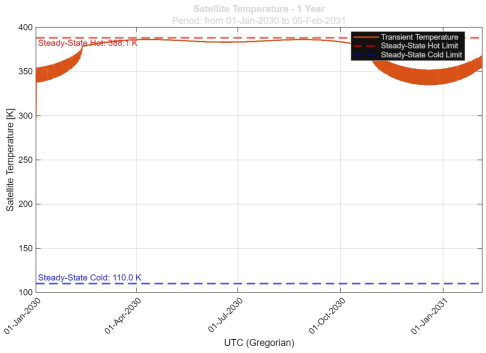

Fig. 41: One-year satellite temperature profile with steady-state hot and cold limits (aluminum finish).

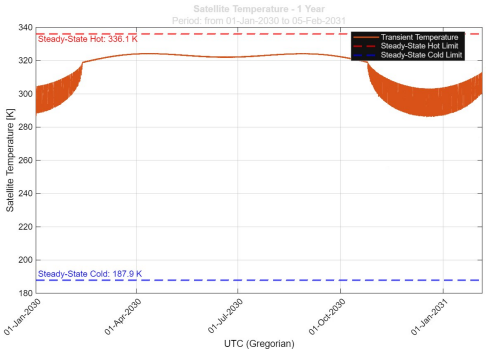

Fig. 42: One-year satellite temperature profile with steady-state hot and cold limits (black coating finish).

configuration led to a more uniform temperature distribution and reduced peak temperatures in the worst-case hot scenario (Fig. 42). The corresponding worst-case hot and cold results for both surface finishes are reported in Table 20.

Table 20: Preliminary worst-case thermal conditions.

Surface Finish	Worst Case Cold	Worst Case Hot
Aluminum (polished)	24.32 °C	113.11 °C
Black-coating	13.17 °C	51.06 °C

Based on these preliminary results, an initial configuration of the thermal control system can be inferred, providing guidance on the selection of suitable thermal control devices to maintain the spacecraft temperature within the required limits.

In the final phase of the thermal analysis, the MATLAB CubeSat Thermal Power Toolbox is employed to increase the fidelity of the thermal model and relax several simplifying assumptions adopted in the preliminary analyses. A multi-node geometry is implemented, allowing temperature gradients across the spacecraft structure and removing the isothermal body assumption. While the solar constant is assumed to be fixed and equal to 1361 W/m^2, the absorbed solar power varies in time as a function of surface orientation and self-shadowing effects, which are explicitly accounted for by the toolbox.

3.6.1 Cubesat Model

After deployment, the CubeSat is modeled as a 3U + 1U configuration. The 3U unit contains the subsystems required for spacecraft survival, whereas the 1U unit accommodates the receiving portion of the payload. For simplicity in the thermal modeling process, the two units are treated as thermally independent, allowing their thermal behavior to be analyzed separately.

- **1U unit (Fig. 43):** the unit is modeled with six external faces, one of which is finished with a black thermal coating while the remaining are in aluminum, and a single internal node. No internal power dissipation is included in this configuration, as the payload housed in the 1U unit operates only during short-duration scientific tests. Consequently, the thermal behavior of the unit is entirely driven by external environmental heat fluxes and by conductive coupling between the internal node and the external surfaces.
- **3U unit (Fig. 44):** a more detailed thermal model is adopted for this unit, as it hosts thermally sensitive payloads and subsystems. Distinct thermo-optical properties are assigned to the external faces, and the presence of deployable solar panels is explicitly accounted for. The surface material selection is the result of multiple iterative simulations, carried out to ensure that both internal and external node temperatures remain within component operational limits under all considered conditions, without the need for active thermal control elements.

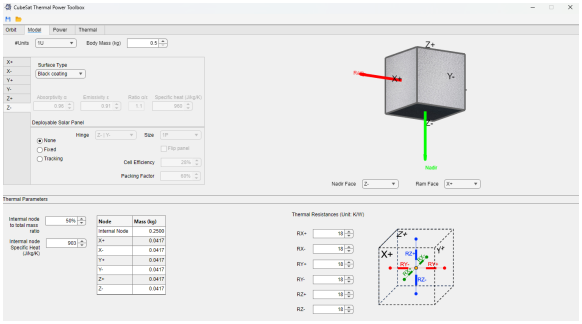

Fig. 43: 1U cubesat model

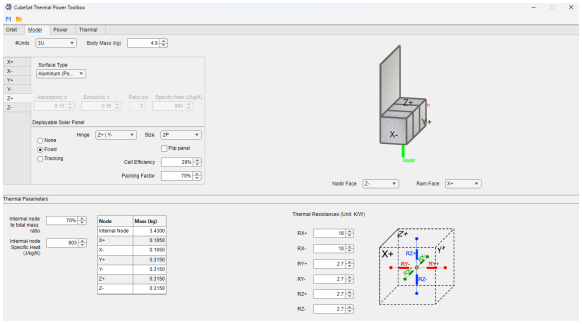

Fig. 44: 3U cubesat model

The materials assigned to each external face are summarized in Table 21.

Table 21: Thermo-optical material assignment for the external faces of the 3U unit.

Face	Surface Material
$X+$	Aluminum (polished)
$X-$	Aluminum (polished)
$Y+$	White thermal coating
$Y-$	Solar panel
$Z+$	Aluminum (polished)
$Z-$	White thermal coating

3.6.2 Results

This section presents the simulation results obtained over the first three months of on-orbit operation. In particular, Fig. 45 shows the internal temperature evolution of the 1U unit, while Fig. 46 and Fig. 47 report the internal temperature and the external surface temperatures of the 3U unit. For the latter, special attention is given to the temperature of the y- face, where the solar panels are located. Subsequently, Table 22 summarizes the corresponding worst-case thermal conditions by highlighting the maximum and minimum temperatures extracted from the distributions shown in the figures.

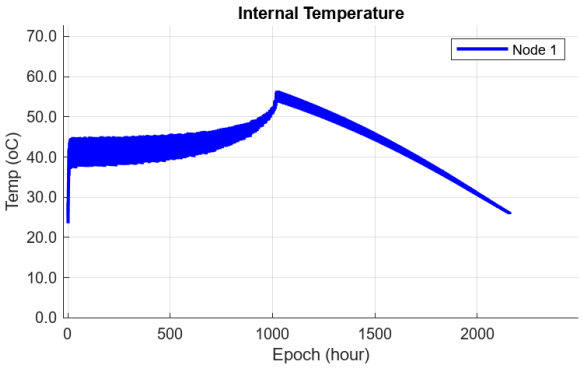

Fig. 45: Internal temperature the 1U unit.

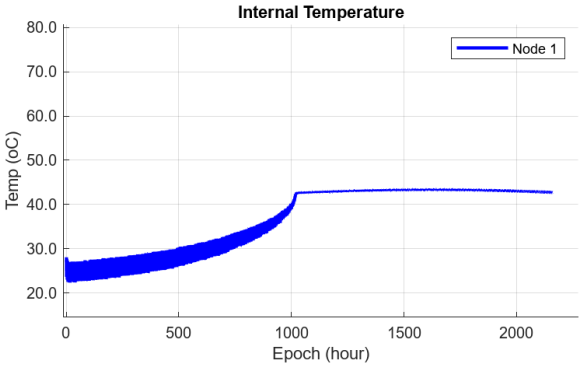

Fig. 46: Internal temperature the 3U unit.

Table 22: Worst-case thermal conditions.

	Worst Case Cold	Worst Case Hot
1U T_{internal}	23.37 °C	56.36 °C
3U T_{internal}	22.17 °C	43.24 °C
$T_{\text{solar panels}}$	10.3 °C	76.54 °C

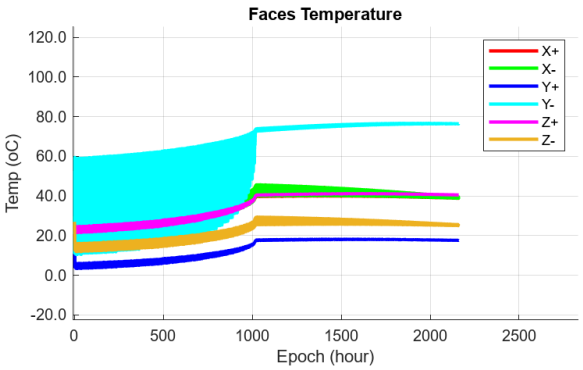

Fig. 47: Surfaces temperature the 3U unit.

3.6.3 Thermal Requirements Verification

To assess whether the thermal control system is adequately effective using passive measures alone, or whether additional mitigation strategies are required, the predicted worst-case temperatures are compared against the allowable operating temperature ranges of the critical components, as listed in the Table 23.

As expected from the adopted passive thermal control system design, the predicted temperatures at the internal nodes and on the solar panel surfaces remain within the allowable operational limits of all considered components. Consequently, at this stage of the spacecraft design, no active thermal control measures are considered necessary for further thermal management.

Note that, these conclusions are necessarily tied to the schematic level of the present satellite model. A more detailed definition of the internal component layout and of the associated heat fluxes may require refinements of the thermal control strategy, including localized insulation of thermally sensitive components and, if needed, the introduction of active thermal control elements.

3.7 Radiation Environment Analysis

The space radiation environment represents one of the most critical challenges for satellite missions, as it directly affects the durability and functionality of onboard components. At the operational altitude of 450 km in a Sun-Synchronous Orbit (SSO), the POWER CubeSat is exposed to a complex combination of radiation sources, more specifically, to particles trapped in the Earth's magnetosphere (protons and electrons). The intensity of these sources varies significantly as a function of altitude, orbital inclination, and solar activity.

To ensure mission success, it is essential to evaluate the total radiation dose that the satellite will experience over its operational lifetime. The analysis was carried out using the SPENVIS (Space Environment Information System) software, which allows modeling of the radiation environment, estimation of absorbed doses, and assessment of the shielding requirements needed to protect sensitive components.

The characterization of the environment is defined by the flux of charged particles and their corresponding energy levels. For this analysis, standard industry models were employed: AP-8 for protons and AE-8 for electrons, both set to MAX mode to reflect the expected solar maximum conditions.

By inputting the orbital parameters of the POWER mission (450 km altitude, 97.2° inclination), the software calculated the averaged proton and electron fluxes:

- Protons: The integral flux calculated for energies greater than 0.10 MeV is equal to 5.4436×10^2 $cm^{-2}s^{-1}$. The flux decreases significantly with increasing energy, dropping to 1.2756×10^1 $cm^{-2}s^{-1}$ for energies above 10 MeV.

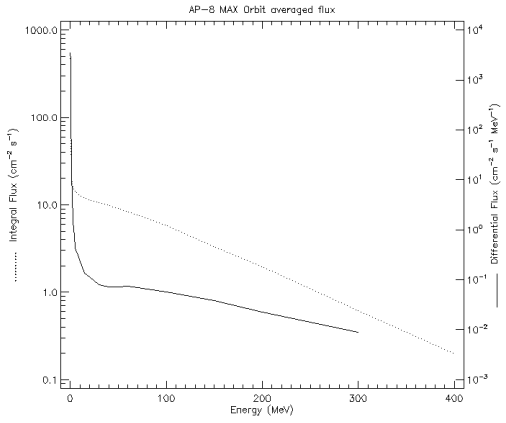

Fig. 48: Averaged spectra of trapped protons

Table 23: List of Components with Operational Temperatures.

Subsystem	**Component**	T_{min} **(°C)**	T_{max} **(°C)**
Payload	Supercapacitor	-40	65
	Variable Step-Down Reg.	-40	125
	Sync. Boost Converter	-40	125
	VCO	-40	85
	RF-to-DC (Rectenna)	-65	150
	DC/DC Converter	-40	125
	Transmitting Antenna	-40	125
	Receiving Antenna	-40	125
	Power Amplifier	-40	50
ADCS	ADCS Box	-35	70
EPS	Battery Pack	0	50
	PCDU - Dock	-35	85
	Array Conditioning Unit	-35	85
	Power Distribution Unit	-35	85
	Solar Panels	-40	80
	Solar Panels (deployed)	-40	80
TT&C	Transceiver	-25	85
	Antenna	-20	50
OBDH	OBC	-30	85
TCS	TBC	—	—

- Electrons: The electron flux is significantly higher, with an integral value of 1.3418×10^5 $cm^{-2}s^{-1}$ for energies greater than 0.04 MeV.

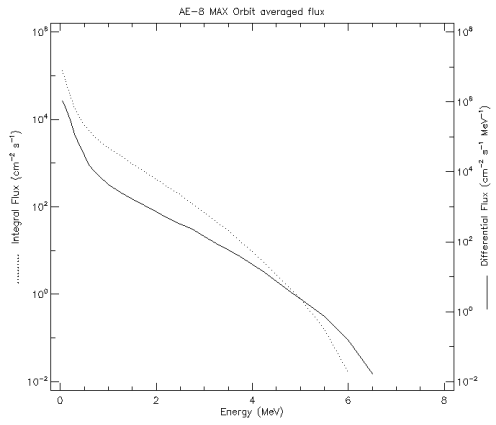

Fig. 49: Averaged spectra of trapped electrons

The selected cells (Triple Junction GaAs Azur 3G30) were simulated with a front shielding thickness of 100 μm (cerium-doped borosilicate coverglass). The results show a 1 MeV equivalent electron fluence on the order of 10^{10} cm^{-2} after 365 days of mission. Since this value is significantly lower than the critical damage threshold for 3G30 cells (typically $> 10^{14}$ cm^{-2}), the maximum power degradation factor ($P_{\max}$) is negligible ($< 1\%$). Consequently, for the POWER mission energy budget, there is no need to oversize the solar panels to compensate for radiation damage during the first year.

The Total Ionizing Dose (TID) analysis was performed to assess the effectiveness of aluminum shielding against the orbital radiation environment. The results, obtained using the SHIELDOSE-2 model and summarized in Fig. 50, show the absorbed dose in silicon (rad(Si)) over a 365-day mission period, considering absorber thicknesses ranging from 1.0 mm to 2.5 mm.

The data highlight a strong sensitivity of the total dose to the shielding thickness, primarily

driven by the electron component. For a thickness of 1.0 mm, the annual total dose amounts to 581.74 rad, with more than 94% (551.95 rad) attributed to trapped electrons. Increasing the thickness to 1.5 mm results in a 49% reduction of the dose, yielding 296.06 rad. In this configuration, although the electron flux remains the dominant source, the effectiveness of structural attenuation is clearly evident.

As the thickness is further increased to 2.5 mm, the total dose decreases to 103.50 rad. Beyond 2.0 mm, a change in the attenuation profile is observed: while the contribution from electrons and bremsstrahlung radiation continues to decrease significantly, the contribution from trapped protons exhibits a much slower reduction, decreasing from 25.98 rad (at 1.0 mm) to 19.58 rad (at 2.5 mm).

In conclusion, the analysis demonstrates that an overall shielding thickness of 2.5 mm provides a benign radiation environment for onboard electronics, reducing the annual exposure by more than 80% compared to a minimal 1.0 mm shielding and offering a substantial safety margin with respect to the typical tolerance thresholds of COTS components.

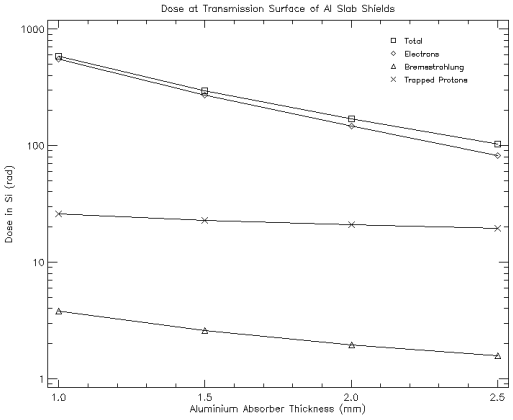

Fig. 50: Dose as a function of shielding thickness

4 Conclusion

The POWER mission represents a significant step forward in the validation of Wireless Power Transfer technologies for space applications using a nanosatellite platform. The conceptual design presented in this paper demonstrates the feasibility of integrating a high-power microwave transmission payload within the strict size, weight, and power (SWaP) constraints of a 3U CubeSat.

Key achievements of this Phase A study include the definition of a rail-based deployable architecture that mitigates the complexities of formation flying while ensuring precise alignment for WPT experiments. The preliminary electrical power analysis confirms that the proposed hybrid storage system, combining standard Li-Ion batteries with a supercapacitor bank, is capable of managing the 19.4 W peak load required during transmission bursts, maintaining a healthy Depth of Discharge on the main bus. Furthermore, the thermal and radiation analyses validate the resilience of the selected commercial-off-the-shelf (COTS) components in the reference 450 km Sun-Synchronous Orbit, with a passive thermal control strategy proving sufficient to keep all subsystems within operational limits.

While the current work establishes a solid baseline for the mission feasibility, future Phase B activities will focus on the consolidation of the detailed design, the breadboarding of the RF rectification chain, and the mechanical qualification of the deployment mechanism. Ultimately, POWER aims to pave the way for a new generation of service satellites capable of extending the operational life of orbital assets, directly contributing to a more sustainable and efficient use of the space environment.

References

[1] Ayling, A., Fikes, A., Mizrahi, O.S., Wu, A., Riazati, R., Brunet, J., Abiri, B., Bohn, F., Gal-Katziri, M., Hashemi, M.R.M., *et al.*: Wireless power transfer in space using flexible, lightweight, coherent arrays. Acta Astronautica **224**, 226–243 (2024)

[2] European Space Agency: Supercapacitors Ready to Deliver Maximum Power to Space. Accessed: 2025-01-16

[3] European Space Agency: SpaceCap Supercapacitor Series Solves Power Problems. Accessed: 2025-01-16

[4] United Nations: Sustainable Development Goals. Accessed: 2025-01-16

[5] Brooks, D.R.: An introduction to orbit dynamics and its application to satellite based earth monitoring missions. Reference publication, NASA, Hampton, Virginia (1977)

[6] Duck, K.I., King, J.: Orbital mechanics for remote sensing. In: Manual of Remote Sensing vol. 1. American Society of Photogrammetry, Virginia (1983)

[7] European Space Agency: ESA's Zero Debris Approach. Accessed: 2026-01-05. https://www.esa.int/Space_Safety/Clean_Space/ESA_s_Zero_Debris_approach

[8] Rollco: Telescopic Rail Heavy ASN22. Accessed 13 January 2026. https://www.rollco.eu/products/telescopic-rail-heavy/telescopic-rail-heavy-asn-22

[9] SODEMANN Industrial Springs: A480-029-050 Conical Spring. Accessed 13 January 2026. https://www.industrial-springs.com/a480-029-050

[10] Cicoil: Cicoil Flat Cable. Accessed 13 January 2026. https://www.cicoil.com/flat-cable/learn-more

[11] The CubeSat Program: CubeSat Design Specification (CDS) REV 14.1. California Polytechnic State University, San Luis Obispo, CA (2022). California Polytechnic State University. Accessed: 13 January 2026. https://www.cubesat.org/s/CDS-REV14$_1$ − 2022 − 02 − 09.*pdf*

[12] G.A.U.S.S. Srl: G.A.U.S.S. Srl – CubeSat Deployer GPOD. Accessed: 13 January 2026. https://www.gauss.space/products/#dep

[13] CNES – Centre National d'Etudes Spatiales: IDM Tools – Presentation. Accessed: 2026-01-14. https://www.idm-tools.com/presentation

[14] Walker, R.: System Margin Policy for ESA IOD CubeSat Projects. Policy Document TEC-SY/77/2016/POL/RW, European Space Agency (ESA) (February 2016). Issue 1, Revision 0

[15] SRE-PA & D-TEC staff: Margin philosophy for science assessment studies. Technical Note SRE-PA/2011.097/, European Space Agency (ESA) (June 2012). Issue 1, Revision 3

[16] Mithil, A.S., Shankar, S., Sameera, T.N., Kumar, R.: Design and implementation of reconfigurable microwave wireless power transfer systems for small-scale applications. In: Proceedings of an International Conference on Electronics and Communication Engineering, Dharwad, Karnataka, India (2024)

[17] Balanis, C.A.: Antenna Theory: Analysis and Design, 4th edn. John Wiley & Sons, Hoboken, NJ, USA (2016)

[18] Kar, P.C., Islam, M.A.: Design and performance analysis of a rectenna system for charging a mobile phone from ambient em waves. Heliyon **9**(3), 13964 (2023) https://doi.org/10.1016/j.heliyon.2023.e13964

[19] Gonzalez-Llorente, J., Lidtke, A.A., Hatanaka, K., Limam, L., Fajardo, I., Okuyama, K.-I.: In-orbit feasibility demonstration of supercapacitors for space applications. Acta Astronautica **174**, 294–305 (2020)

[20] Kalbitz, R., Puhane, F.: Supercapacitor – A Guide for the Design-In Process. Würth Elektronik, (2020). Würth Elektronik. Application Note ANP077

[21] Eaton: TV Supercapacitors.Technical Data 10554. Eaton, (2024). Eaton. https://www.eaton.com

[22] Aburouk, T., Kim, S., Masui, H., Cho, M.: Design, fabrication, and testing of an electrical double-layer capacitor-based 1u cubesat electrical power system. Journal of Small Satellites (JoSS) **7**(1), 701–717 (2018)

[23] Linear Technology: LT3971/LT3971-3.3/LT3971-5 38V, 1.2A, 2MHz Step-Down Regulator with 2.8A Quiescent Current. Linear Technology, (2009). Linear Technology. Model: TV1860-3R0107-R

[24] Linear Technology: High Efficiency, Synchronous, 4-Switch Buck-Boost Controller. Linear Technology, (2010). Linear Technology. Model: TV1860-3R0107-R

[25] SkyLabs: NANOlink SDR S-Band Transceiver Datasheet. SkyLabs, (2020). SkyLabs. nano-link-base-sb-1 / nano-link-boost-sb-1

[26] ISISPACE Group: CubeSat S-Band Patch Antenna Datasheet. ISISPACE Group, Delft, The Netherlands (2021). ISISPACE Group

[27] National Aeronautics and Space Administration: Near earth network (nen) users' guide. Technical Report 453-NENUG, Revision 5, NASA Goddard Space Flight Center, Greenbelt, Maryland, USA (March 2019). Near Earth Network Project, Code 453

[28] Asundi, A., Sharan, G., Norman, G., Fitz-Coy, N.: Design of command, data and telemetry handling system for a distributed computing architecture cubesat. In: Proceedings of the 2013 IEEE Aerospace Conference. IEEE, ??? (2013)

[29] GomSpace: NanoMind A3200 – Onboard Computer. Accessed: 13 January 2026. https://gomspace.com/shop/subsystems/command-and-data-handling/nanomind-a3200.aspx

[30] NASA Jet Propulsion Laboratory: F' (F Prime) – A Flight Software Framework. Accessed: 13 January 2026. https://fprime.jpl.nasa.gov/

[31] Endurosat: 3U Deployable Solar Array. Accessed 5 January 2026. https://www.endurosat.com/products/3u-deployable-solar-array/

[32] GomSpace: NanoPower BP4 3000mA - Datasheets. (2018). GomSpace. Document No.: 1013024 - Approval date: 10 October 2018

[33] GomSpace A/S: NanoPower P60 Dock - Datasheet. (2024). GomSpace A/S. Doc. No. 1013119, Rev. 3.0

[34] GomSpace A/S: NanoPower P60 ACU-200 - Datasheet. (2018). GomSpace A/S. Doc. No. 1014406, Rev. 2.3

[35] ECSS Secretariat: Space Engineering – Electrical and Electronic. European Cooperation for Space Standardization (ECSS). https://ecss.nl/standard/ecss-e-st-20c-rev-2-electrical-and-electronic-8-april-2022/